An Apparatus for Frequency Resolved Optical Gating of Attoseconds Pulses

by

Alexander Visotsky Soane

B.S. Physics
Massachusetts Institute of Technology, 2009

Submitted to the Department of Electrical Engineering and Computer Science
in partial fulfillment of the requirements for the degree of

Master of Science in Electrical Engineering and Computer Science

at the

MASSACHUSETTS INSTITUTE OF TECHNOLOGY

February 2011

Author .....
Department of Electrical Engineering and Computer Science
January 28, 2011

Certified by .....
Franz Kärtner
Professor of Electrical Engineering and Computer Science
Thesis Supervisor

Accepted by .....
Terry P. Orlando
Chairman, Department Committee on Graduate Students

An Apparatus for Frequency Resolved Optical Gating of Attoseconds Pulses

by

Alexander Visotsky Soane

B.S. Physics

Massachusetts Institute of Technology, 2009

Submitted to the Department of Electrical Engineering and Computer Science
on January 28, 2011, in partial fulfillment of the
requirements for the degree of
Master of Science in Electrical Engineering and Computer Science

Abstract

I report on the design and construction of an apparatus for frequency resolved optical gating of attosecond pulses. Frequency resolved optical gating is the state-of-the-art technique for measuring the temporal profile of attosecond optical pulses. In this thesis, I discuss the operation of the apparatus in the context of the theoretical background, numerical algorithms, and engineering design features of the experimental system.

This thesis contains detailed explanations of the various design goals and decisions that are necessary to understand in order to successfully operate the system.

Thesis Supervisor: Franz Kärtner
Title: Professor of Electrical Engineering and Computer Science

Acknowledgments

I would like to thank Professor Franz Kärtner, who has been a source of guidance and support. I am grateful for the opportunity to work with him at MIT.

Thank you Donnie Keathley, the best colleague and a personal friend.

My acknowledgement also extends to all of my colleagues in the Optics and Quantum Electronics group. To Chien-Jen, I thank him for teaching us how to be HHG experimenters. To Jeff Moses, I recognize the many conversations we had about attosecond science and optics in general. The list of my thanks is numerous and includes everyone at the OQE.

My brother, Nicky Soane, Civil Engineering student at MIT, will always be a stabilizing presence in my life.

My parents, Drs. David and Zoya Soane, who have always had faith in me.

My grandmother, Galina Arkadievna, whose memory serves as an inspiration at MIT.

Contents

List of Tables

List of Figures

Chapter 1

Introduction

High Harmonic Generation (HHG) is an expanding field of research with a wide range of applications. HHG is a nonlinear process by which a fundamental frequency of light is upconverted via a medium to a higher harmonic. HHG has allowed researchers to break the "femtosecond barrier" by achieving light pulse durations on the order of attoseconds. The latest success of this field traces its lineage over an exciting history of optics research. Beginning in the 19th century, the control of light waveforms allowed for a selection of intensity, duration, and synchronization between pulses. Since its inception, this ability to control light has been a valued tool for both fundamental science and engineering. The graph in Fig. 1-1 shows the shortest pulse duration plotted against year, which aptly demonstrates the rapid progress made in the field of ultrafast optics.

One of the principle challenges of attosecond pulse generation is the accurate measurement of the temporal characteristics of the pulses. Although the magnitudes of frequencies comprising an attosecond pulse are measurable with a spectrometer, it is necessary to also know the relative phase of these frequencies in order to reconstruct the temporal profile of the pulse. In recent years, the field of HHG has produced cutting-edge technologies for determining the phase of an attosecond pulse.

In this thesis, I report on the construction of an apparatus designed to measure the temporal profile of optical pulses on the order of attoseconds. The relevant numerical recipes that are fundamental to the measurement system are also discussed. This

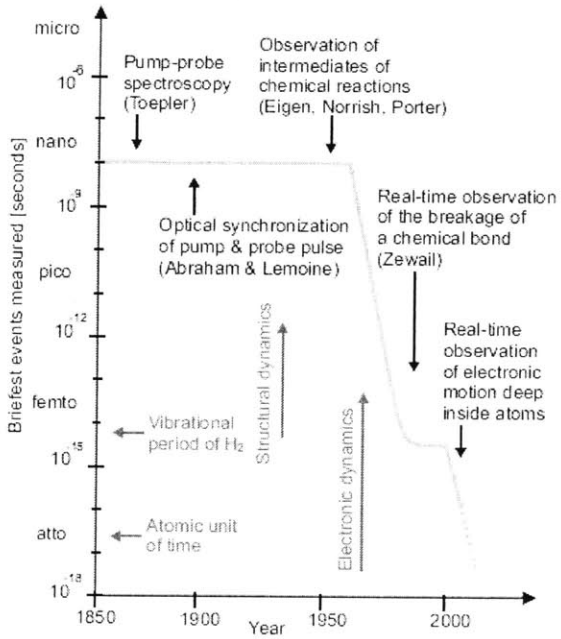

Figure 1-1: This graph shows the evolution of minimum pulse durations as a function of year. Graph taken from [ ].

original work was performed a collaboration with the author's colleague Phillip D. Keathley, a graduate student in the Optics and Quantum Electronics group at MIT. The scope and breadth encompassed by this research project was significantly diverse such that an equal and productive in a collaboration yielded beneficial results. This thesis is organized as follows. A brief summary of the theory of the pertinent subjects in high harmonic generation and phase retrieval schemes forms the introductory material for the thesis. In the following discussion, an explanation of the numerical recipes motivates and complements the setup of the apparatus. Finally, the core body of the thesis focuses on the engineering design and considerations invested in the construction of the experimental layout and apparatus.

Chapter 2

Theory of High Harmonic Generation

HHG is a highly nonlinear process in which an atomic medium (typically nobel gases) interacts with a driving laser field to upconvert the light to much higher frequencies. The structural framework for understanding HHG is presented in this section.

2.1 Coherence

At its heart, HHG is a quantum mechanical phenomenon, but the extension to the semi-classical regime is analytically and experimentally valid [2, 1, 3, 4]. Thus, to understand HHG, it is best to approach the process from a semi-classical viewpoint. Electrons that undergo energy level transitions in atoms may release photons. The energy (frequency) of emitted photons is related to the change in the energy of the electron. A free electron that combines with an ion releases energy in an amount called the *ionization potential*. From a theoretical standpoint, if we ignore scattering effects when a moving electron combines with an ion, any kinetic energy contained in the free electron is included in the quanta of energy emitted. Thus, it is possible for a combination event to release a photon of energy greater than the ionization potential alone. This forms the basis for the semi-classical interpretation of HHG.

Already, we see that it is possible by firing electrons at ions to induce transitions

that emit high energy photons. Although this is technically feasible, the advantages of such an "electron gun" for generating high energy photons is limited. This is because of the concept of *coherence*. In the scenario described, the actual combination event is a random process. The electrons have unique flight paths, so the phase of any two given electrons may be spatially and temporally uncorrelated. Since the electron imparts its phase to the emitted photon, this means that the generated light is comprised of uncorrelated photons. Thus, the light is incoherent spatially and temporally. To produce attosecond duration pulses, it is necessary to have a source of coherent light. Coherent light may be added together to make short pulses.

2.2 Three Step Model

The solution to the problem of generating coherent light is to use a coherent electron "source". On the energy scale necessary to create attosecond pulses, creating a coherent electron source is a challenge. HHG solves this problem by using an already coherent light source from a laser to drive the motion of electrons. The physics of this process are typically treated under the assumptions of the Strong Field Approximation (SFA), which neglects the Coulomb potential of ions in the presence of a strong, external electric field. Thus, free electrons in a plasma will only "see" the externally generated electric field and not the Coulomb potential due to other charges in the vicinity. This approximation allows us to use classical electrodynamics to account for the motion of free electrons in such a medium. The resulting semi-classical explanation of harmonic generation is known as the Three Step Model, which is schematically shown in Fig. 2-1.

In the first step, we begin by considering a single atom. Neglecting inter-atomic interactions is valid because of both the SFA and the use of dilute gas as a generation medium. The process begins by bathing the neutral atoms in an intense, infrared (IR) femtosecond pulse. The exact intensity of the IR may be chosen such that its electric field is on the order of the strength of the Coulombic electric field. This implies the Stark Effect, which describes the dynamics of a bound electron under the influence

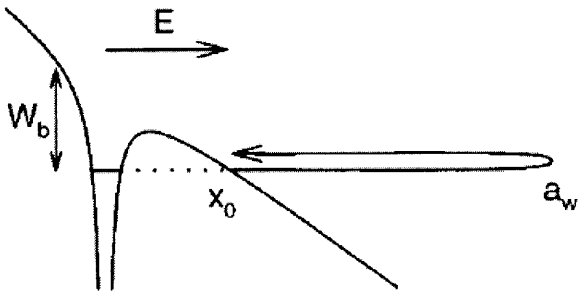

Figure 2-1: Schematic showing the effect of the IR electric field changing the shape of the Coulombic potential well. This allows the electron to tunnel through the ionization barrier of I_p (here shown as W_p). The electron trajectory is determined by the IR electric field with a turning point at a_w. Upon recombination, the electron transfers its kinetic energy plus the ionization potential to an emitted photon of energy greater than the ionization energy. Figure taken from [ ].

of a strong, external field. With the assumption of a "single active electron" (only the valence electron has a change in its wavefunction), then the intense IR field may induce a tunneling event.

It is important to note that electron tunneling describes the dynamics of the electron's wavefunction. Strictly speaking, it is incorrect to assume that an electron has either tunneled or not. Thus, when the IR causes the valence electron to tunnel, this is represented mathematically as a split in the electron's original ground state wavefunction:

$$|\Psi_e\rangle = |\psi_g\rangle \rightarrow |\psi_g\rangle + |\psi_c\rangle \tag{2.1}$$

where g denotes the ground state and c denotes a continuum state (free electron state). For computation purposes, it is assumed that the tunneled "part" of the electron is born with no initial momentum. This is impossible under the Heisenberg Uncertainty Principle, but for ease of analytical evaluation it is an appropriate approximation. Thus, in the SFA regime, the continuum part of the electron's wavefunction may evolve as a free electron wavepacket. This process is the second step of the model. Classically, an electron would be accelerated by the IR's electric field

away from the atom. When the field switches polarity, the classical electron would also change its acceleration and eventually collide with its point of origin - the atom. An oscillating charge in a sinusoidal electric field acquires what is known as the *ponderomotive energy*, calculated to be:

$$U_p = \frac{e^2 E^2}{4m\omega^2} \tag{2.2}$$

where E is the IR field magnitude at the moment of electron tunneling, e is the electron's charge, and ω is the IR frequency. For the case of this electron accelerated by the IR field, trajectory calculations show that when the electron passes by the atom it will have a kinetic energy of about $3.2U_p$ [ ]. In the final step, if the electron recombines with the ion, the emitted photon will have an energy of $\hbar\omega \approx 3.2U_p + I_p$, where I_p is the ionization potential of the atom. As this energy is greater than the simple transition energy of I_p, this shows that the IR pulse has caused the emission of a photon of higher frequency. Alternatively, we can look at the dipole moment of the recombination wavefunction from Eq. 2.1. In particular, the photon emission in this case is related to the expected dipole moment:

$$\langle \vec{d} \rangle \propto \langle \psi_g | e\vec{r} | \psi_c \rangle. \tag{2.3}$$

The form of Eq. 2.3 shows the importance of the transverse structure of $|\psi_c\rangle$, the wavefunction distribution in the direction orthogonal to the IR electric field. It is normally assumed that the transverse components of the free electron wavefunction evolve according to the behavior of a wavepacket in free space [ ]. The dynamics of free wavepacket evolution mirror that of diffusion equations: The wave packet spreads linearly in time in the transverse directions. Thus, the effective amplitude as "seen" by the atom in the transverse overlap of $|\psi_c\rangle$ over the atom's dimension is a function of the time of flight of the electron, which in turn is related to the frequency of the driving IR field. Consequently, although the electron may acquire greater kinetic energy during its flight in a low frequency IR field, the overlap of the recombination amplitude is reduced for the longer time of flight. Maximizing the expected dipole

moment in Eq. 2.3 is one of the challenges of HHG.

Quantum mechanically speaking, the returning continuum wavefunction interferes with the ground state wavefunction (of the same electron). This interference produces a dipole moment as calculated in Eq. 2.3 that is interpreted graphically as the "ripples" caused by the wave function interference, as seen in Fig. 2-2. The dipole moment arises from a time-dependent oscillation of the amplitude of the interference; that is, $|\psi_g + \psi_c|^2$. These high frequency oscillations correspond to oscillations of the electron density, which is the origin of the dipole moment.

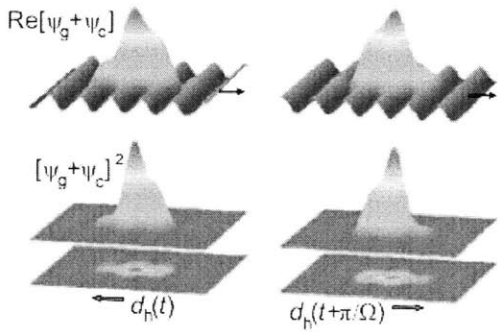

Figure 2-2: Graphical sum of the ground and continuum wavefunctions during interference at recollision. The plot of the real part of this sum shows the fast oscillations that correspond to electron density oscillations. The two plots show the same interference at different times, which indicates the existence of a dipole moment as seen by the amplitude plot. This figure is taken from [1].

The actual harmonic nature of HHG comes from the periodicity of the IR pulse. Electron tunneling from the gas occurs around the peaks of the IR pulse. Each peak of the IR produces, ideally, a burst of high energy photons in a coherent attosecond pulse. Because the neighboring peaks of the IR are opposite in polarity, the resulting attosecond pulses are also opposite in polarity with respect to neighboring pulses. Thus, when considering the train of attosecond pulses resulting from an oscillating IR field, the anti-periodicity of the attosecond pulses with respect to the period of the IR field means that even multiples of the fundamental IR frequency are excluded from the Fourier Series of the attosecond train. The fundamental harmonic of the Fourier Series is the IR frequency, as this is the base period for the train of attosecond

pulses. A schematic of this is shown in Fig. 2-3.

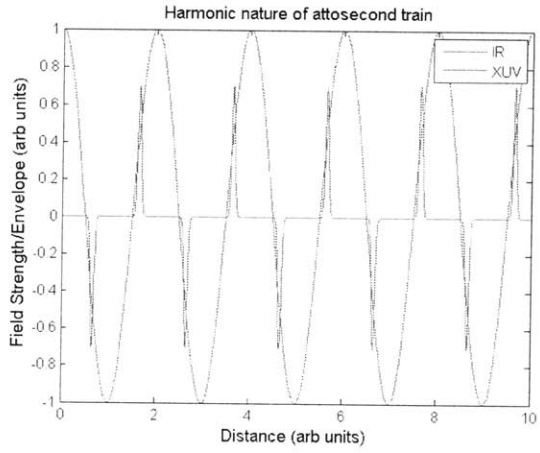

Figure 2-3: The half-wave anti-symmetry of the attosecond envelopes with respect to the IR period restricts the allowed harmonics. Because of the symmetry properties of the Fourier Series, only harmonics of odd multiples (ω, 3ω, 5ω, etc.) exist. Here, the IR pulsed is assumed to be very long in duration such that the amplitude of the field is approximately unchanged.

The duration of the femtosecond IR field determines the number of attosecond pulses in the pulse train. If a high throughput is desired at a certain wavelength range it is possible to use a bandpass filter with the pulse train to obtain a high flux of photons. In some applications, however, a single attosecond pulse may be more useful. Several schemes have been proposed for generating single attosecond pulses. In both the single pulse and pulse train scenarios, it is advantageous to have a tool for measuring the output of HHG in order to verify the temporal profile of the pulses. In the following chapter, we examine the basis and practical implementation of phase retrieval techniques.

Chapter 3

Phase Retrieval

One of the principle challenges of attosecond pulse generation is the accurate measurement of the temporal characteristics of the pulses. Although the magnitudes of frequencies comprising an attosecond pulse are measurable with a spectrometer, it is necessary to also know the relative phase of these frequencies in order to reconstruct the temporal profile of the pulse. In recent years, the field of HHG has produced cutting-edge technologies for determining the phase of an attosecond pulse [ ]. No isolated machines exist that package these technologies on a commercial scale, so it is necessary to understand both the theoretical background and the numerical algorithms that constitute a successful measurement. This chapter explains both aspects of phase retrieval.

3.1 Frequency Resolved Optical Gating

3.1.1 Motivation for Phase Retrieval

Any temporal pulse at a carrier frequency ω_0 may be represented by a complex vector, $\mathbf{A}(t)e^{i\omega_0 t}$, with the relation that the real field $\mathbf{E(t)} = \mathrm{Re}[\mathbf{A(t)}e^{i\omega_0 t}]$. This may be rewritten as

$$\mathbf{A}(t) = |\mathbf{A}(t)| \exp\left(i\omega_0 t - i\phi(t)\right) \tag{3.1}$$

where $\phi(t)$ is the phase of the pulse and ω_0 is the carrier frequency. For simplicity, we will drop two spatial components of the signal and reduce the problem to one spatial dimension ($|\mathbf{A}(t)| \rightarrow |A(t)|$).

Eq. 3.1 is the temporal description of a pulse, which is not measurable in the realm of ultrafast optics. This is because the temporal resolution of instruments cannot capture changes that occur within some minimum time window. Many techniques, such as autocorrelation measurements, exist that may directly measure the pulse width in the time domain. Unfortunately, instrument capabilities limit their use in some ultrafast optical scenarios. In the regime of ultrafast optics, pulses may be far shorter in duration than the fastest instruments can directly capture. Thus, it is necessary to describe pulses in parameters that can be measured with existing equipment.

Spectrometers can be made with very high resolution within the frequency (energy) domain. It is possible to recast Eq. 3.1 into the frequency domain to exploit the high resolution of spectrometers. Conceptually, Eq. 3.1 may be thought of as a multiplication in the time domain of three time-dependent functions: the amplitude $|A(t)|$, the carrier $e^{i\omega_0 t}$, and the phase $e^{i\phi(t)}$. In frequency space, this multiplication becomes a convolution, so the Fourier transform of the pulse is a convolution of three functions in frequency domain. The carrier frequency provides a shift so that the transform is located around ω_0. The amplitude determines the magnitude of each frequency component, and the phase adds a phase term to each frequency. In practice, it is often sufficient to determine the temporal envelope $A(t)$ and to ignore the carrier. If there were a way to measure, in frequency space, the related functions then it is possible to reconstruct $A(t)$.

A spectrometer measures intensity in frequency space, which is proportional to $|\tilde{A}(\omega)|^2$ only. Phase information is not measured. Although we can now determine the magnitude of the frequency components that comprise the pulse, we do not have the phase information necessary to properly reconstruct the envelope $A(t)$ in time. Consequently, it is necessary to devise a method of measuring the phase of each frequency component.

3.1.2 FROG trace

An intensity spectrogram is a set of one-dimensional data, from which it is impossible to extract two independent functions (magnitude and phase) simultaneously. The introduction of a second variable into the measurement process provides the extra dimension that allows us to fully determine the system parameters. Frequency Resolved Optical Gating (FROG) is a technique that marries the high resolution of frequency spectrometers with an additional independent experimental variable. An unknown signal $E(t)$ (sometimes called a "probe" signal) is convoluted with a signal known as a *gate function*, $g(t)$. The act of convolution introduces a *delay time*, τ. A FROG trace $S(\tau, \omega)$ is the Fourier transform of the convolution of E and g. Mathematically, this is described by

$$S(\tau, \omega) \propto |\int_{-\infty}^{\infty} E(t)g(t-\tau)e^{-i\omega t}dt|^2. \tag{3.2}$$

Because S is a function of two variables, it is clear that the measured data will be in a 2x2 matrix form. Generally, the columns of this matrix are individual spectrograms, each separated by a delay $d\tau$ between the signal and gate pulses. Although each entry of the matrix S will be real (because the spectrogram of a signal is a real intensity function $I(\tau, \omega)$), the phase is encoded into the data. This time-frequency data set is like a musical score, which relates the musical notes (frequencies) that comprise a song (signal pulse) by the various temporal delays between them. In such a way, a song may be described by a two-dimensional data set. Similarly, the FROG trace describes a temporal pulse signal.

What remains is to utilize a method for extracting the unknown temporal pulse from this data set, a process called "phase retrieval" or "deconvolution". Fundamentally, Eq. 3.2 encodes the phase in the following mathematical argument:

$$\sqrt{S(\tau, \omega)}\Phi(\tau, \omega) = \int_{-\infty}^{\infty} E(t)g(t-\tau)e^{-i\omega t}dt \tag{3.3}$$

where $\Phi(\tau, \omega)$ is a complex-valued phase function (magnitude is 1). The physical

data available is in the form of Eq. 3.2, in which the phase function $\Phi(\tau, \omega)$ is lost; however, the magnitude of the entries of $S(\tau, \omega)$ may be used in Eq. 3.3 in a numerical deconvolution recipe. Of practical consideration, it is important to note that the gate function $g(t)$ does not need to be shorter than the timescale of $E(t)$. In fact, there are many setups that use $E(t)$, the unknown pulse to be characterized, as the gate function in a FROG experiment, instead of using a shorter pulse for the gate.

3.2 Principal component generalized projections algorithm

In this section, we closely follow the work of Kane [ ] on the *principal component generalized projections algorithm* (PCGPA). Although the experiment and numerical recipe presented were developed for femtosecond pulse characterization, they will serve as important tools for understanding deconvolution algorithms in general. We will show some of the results when PCGPA is applied to attosecond pulses.

3.2.1 Experimental setup

As described in the section on FROG trace generation, the trace is a set of data that has two independent, experimental parameters - the spectrographic frequencies and the time delay that arises from convolution (see Eq. 3.2). In practice, a spectrometer is able to collect high-resolution frequency data at a fast rate. This would correspond to the "slice" of $S(\tau, \omega)$ along the ω axis for a fixed time delay τ. A mechanical delay stage controls the time delay, which allows a spectrometer to collect the frequency information for different delays.

If we set $g(t) = E(t)$, it is possible to use second harmonic generation (SHG) in a FROG setup. Fig. 3-1 shows the experimental layout in the SHG configuration.

SHG is directly proportional to the intensity of the fundamental field within the nonlinear crystal. When $g(t) = E(t)$, the output of SHG depends on how well-overlapped the pulses are. The mathematical expression in Eq. 3.2 is exactly the

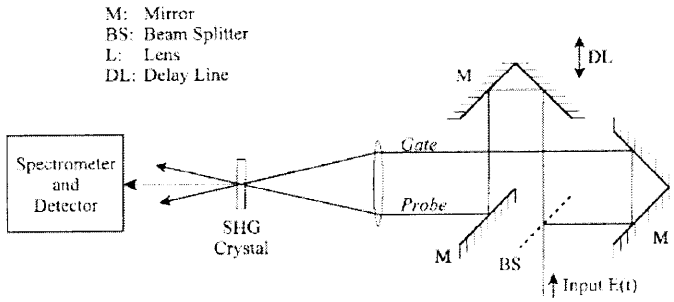

Figure 3-1: A FROG experiment organized to operate with SHG. In this example, the gate and pulse signals are equivalent. A mechanical stage scans through different time delays. The amplitude of the output from the SHG crystal is directly proportional to the intensity of the fundamental field inside the crystal, which allows us to measure the overlap of the gate and pulse. This figure is taken directly from Kane [ ].

Fourier transform of a second harmonic generated by a fundamental field that is delayed by τ. Thus, the SHG signal becomes a measuring tool that can be used in the FROG trace measurement. A mechanical stage changes the time delay τ between the two pulses. At each delay step, the SHG signal is measured by a spectrometer, which is equivalent to one column of the FROG trace matrix S.

3.2.2 Numerical recipe

Despite the name "phase retrieval", all FROG characterization algorithms begin by guessing time-domain field solutions and then enforcing two constraints: intensity and outer product uniqueness. The guessed solutions are vectors with elements corresponding to field values along discretized time. It is a consequence of the mathematical definition of the FROG trace S that the matrix of data generated from a pulse (or "probe") signal and a gate function signal is almost guaranteed to be unique [ ]. As a working assumption, this implies that for time vectors $E_{probe}(t)$ and $E_{gate}(t)$ we will have a unique matrix $S(\tau, \omega_0)$, a property that we may call the "outer product" constraint. It suffices to guess a correct set of probe and gate vectors (pulses in time) that would hypothetically generate the measured FROG trace and rely on the uniqueness of FROG. This "pseudo-guarantee" does not preclude local minimums in

a numerical recipe, and algorithms may converge to unphysical solutions in certain situations.

The origin of the outer product constraint is in the Fundamental Theorem of Algebræ[10]. If we have a one-dimensional set of data represented by a vector $[f_1, f_2, \ldots, f_N]$, we may find a corresponding Fourier transform such that the kth element is

$$F_k = \sum_{m=1}^{N} f_m e^{-2\pi i m k/N} \tag{3.4}$$

with m as the time index. Using the relation $z = e^{-2\pi i m k/N}$, Eq. 3.4 becomes

$$F_k = \sum_{m=1}^{N} f_m z^m. \tag{3.5}$$

Because Eq. 3.5 is a polynomial of one variable, by the Fundamental Theorem of Algebræit may be factored. Thus,

$$F_k = f_N(z - z_1)(z - z_2)\cdots(z - z_N). \tag{3.6}$$

In Eq. 3.6, f_N is a function of the product of the factors. It is not immediately clear that another function g_N of z will be equal to F_k; however, by analogy to the FROG trace we must consider the quantity $|F_k|$. In this situation, if we replace $(z - z_1) \rightarrow (z - z_1)^*$, the complex conjugate, we have just created a new function g_N that is equal to $|F_k|$, because the absolute value makes any number real on the RHS.

The FROG trace generated by Eq. 3.2 is a two-dimensional data set. By analogy with Eq. 3.4, we may write a two-dimensional data set as a polynomial of two variables:

$$F_{k,h} = \sum_{m,n=1}^{N} f_{m,n} z^m y^n. \tag{3.7}$$

Eq. 3.7 is not guaranteed to be factorable, because the theorem only guarantees that polynomials of one variable are factorable. Thus, it becomes practically negligible that another function will satisfy Eq. 3.7, although it is technically possi-

ble. Consequently, the "pseudo-guarantee" of the uniqueness of the FROG trace is a working assumption.

All FROG characterization algorithms begin with a guess of probe and gate pulses in the time domain. Then, the algorithm constructs the corresponding FROG trace and compares the generated trace to the measured trace $S(\tau, \omega_0)$. The guessed vectors are modified based on constraints determined by the measured trace, and a new set of probe and gate vectors are screened by the algorithm. This cycle continues until a numerical tolerance is reached and the algorithm converges to a solution.

Although the entries of the measured FROG trace are real, as previously described, their numerical values are determined in part by the phase of each frequency component. The complex values of the probe and gate vectors encode the phase of the optical pulses. When the algorithm constructs a FROG trace from input guess vectors, the resulting matrix may be complex-valued. Complex-valued entries in the generated FROG trace matrix are a clear indication that the guessed probe and gate vectors are not the true optical pulses, because by the uniqueness assumption there must exist a set of probe and gate vectors that are the solution to the measured data. Replacing the *absolute value* of each entry in the generated FROG matrix with the corresponding real-valued entry from the measured FROG data, we ensure that the *intensity* of the guessed vectors are what the real optical pulses should have. This enforces the physical constraint of the measured intensity. What is not enforced by this substitution is the phase information. Using the updated FROG matrix, the algorithm retrieves an updated pair of probe and gate vectors to generate a new FROG matrix, which is again checked against the measured data. A schematic of this process is shown in Fig. 3-2.

As stated previously, PCGPA begins with a guess for probe and gate pulses in the time domain. Assuming a constant discretization of Δt, the probe and gate pulses may be written as the following vectors:

$$E_P = [P(-\frac{N}{2}\Delta t), P(-(\frac{N}{2}-1)\Delta t), \ldots, P((\frac{N}{2}-1)\Delta t)] \tag{3.8}$$

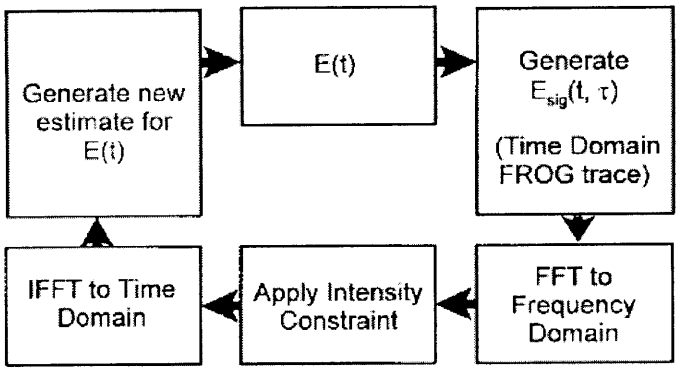

Figure 3-2: This flow diagram illustrates the general steps in a FROG characterization algorithm. The algorithm begins with a guess of probe and gate pulses in time domain. These signals are used to generate a FROG trace in the frequency domain. Intensity from the measured FROG data is applied as a constraint on the amplitudes of the entries of the *generated* FROG trace. The phase of each entry in the matrix is not changed. From this modified matrix new probe and gate pulses are numerically computed from a set of possible vectors. The selected vectors are used to generate a new FROG trace, which is again compared with the measured data. This schematic is taken from [ ].

$$E_G = [G(-\frac{N}{2}\Delta t), G(-(\frac{N}{2}-1)\Delta t), \ldots, G((\frac{N}{2}-1)\Delta t)] \tag{3.9}$$

where E_P and E_G are the probe and gate pulses, respectively. N is the total number of time samples (the length of the vectors) and the functions $P(t)$ and $G(t)$ are the temporal descriptions of the probe and gate pulses. Because there are N total elements, it is simpler to rewrite Eqs. 3.8 and 3.9 in an *outer product* form:

$$E_P = [P_1, P_2, \ldots, P_N] \tag{3.10}$$

$$E_G = [G_1, G_2, \ldots, G_N] \tag{3.11}$$

$$E_P^T E_G = \begin{bmatrix} P_1G_1 & P1G_2 & \cdots & P_1G_N \\ P_2G_1 & P_2G_2 & \cdots & P_2G_N \\ P_3G_1 & P_3G_2 & \cdots & P_3G_N \\ \vdots & \vdots & \ddots & \cdots \\ P_NG_1 & P_NG_2 & \cdots & P_NG_N \end{bmatrix} \tag{3.12}$$

Eq. 3.12 is a useful way to store data in a matrix form. Mathematically, we know that the matrix in Eq. 3.12 must be the outer product of a single pair of vectors. As discussed in [10], there is no other pair of vectors that can form this matrix via an outer product. This fact will be used to find the real E_P and E_G. Additionally, rearrangement of the entries of the outer product matrix leads directly to the matrix form of the FROG trace. This can be seen by examining Eq. 3.2, in which for a fixed delay time τ we can write the integrand (in the time domain) as a vector whose entries are products of shifted elements from E_P and E_G. We discretize the delay time into constant steps of $\Delta\tau$. As an example, for a delay of $-\Delta\tau$, inside the integral would be the vector

$$[P_1G_2, P_2G_3, P_3G_4, \ldots, P_NG_1]. \tag{3.13}$$

The intensity of the Fourier transform of Eq. 3.13 is the column of $S(\tau, \omega)$ that corresponds to the delay of $-\Delta\tau$. We can write N such vectors for the N possible delay times (multiples of $\Delta\tau$). The interesting consequence of using the outer product form (Eq. 3.12) is that every element of the matrix appears as an element of some delay offset vector (as in Eq. 3.13). Thus, with a rearrangement of the entries in Eq. 3.12, it becomes possible to construct a *time-domain* FROG trace.

With the convention that the order of the columns of the FROG trace to correspond to an *increasing* time delay, we write the FROG trace in the time domain:

$$[\tau = \ldots, \tau = -2\Delta\tau, \tau = -\Delta\tau, \tau = 0, \tau - \Delta\tau, \tau = 2\Delta\tau, \ldots] \tag{3.14}$$

$$\text{FROG(time)} \Rightarrow \begin{bmatrix} \cdots & P_1G_3 & P_1G_2 & P_1G_1 & P_1G_N & P_1G_{N-1} & \cdots \\ \cdots & P_2G_4 & P_2G_3 & P_2G_2 & P_2G_1 & P_2G_N & \cdots \\ \cdots & P_3G_5 & P_3G_4 & P_3G_3 & P_3G_2 & P_3G_1 & \cdots \\ \cdots & P_4G_6 & P_4G_5 & P_4G_4 & P_4G_3 & P_4G_2 & \cdots \\ \cdots & P_5G_7 & P_5G_6 & P_5G_5 & P_5G_4 & P_5G_3 & \cdots \\ \cdots & \cdots & \cdots & \cdots & \cdots & \cdots & \ddots \end{bmatrix} \tag{3.15}$$

As each entry in Eq. 3.15 appears in Eq. 3.12, we can use simple rearrangement of entries to convert the outer product form into the time-domain FROG trace. Once put into the time-domain form, the Fourier transform of each column (constant delay τ) is an equation of the form Eq. 3.3. By replacing the magnitude of each transformed entry with that of the corresponding $\sqrt{S(\tau,\omega)}$, we enforce the *intensity* constraint.

Once the intensity constraint has been applied, it is evident that the matrix is now changed. The phase of each entry is preserved, but the altered magnitude of each entry signifies that no longer will the guessed E_P and E_G make an outer product that can be rearranged into the same FROG trace. By the uniqueness argument, if the alternate FROG trace is the physical trace (the phases are correct), then there must exist an unique pair of vectors whose outer product is related to the found FROG trace. In other words, there is a single *principal component* in the singular value decomposition of the FROG trace.

Using a singular value decomposition on the FROG trace M, we can rewrite M as a multiplication of three matrices,

$$M = U\Sigma V^T \tag{3.16}$$

where U is a matrix whose columns are *left-singular* vectors of M, V^T is a matrix whose rows are *right-singular* vectors of M, and Σ is a diagonal matrix with *singular values* along its diagonal. Schematically, M is the sum of N different outer product matrices formed from the left and right vectors of U and V^T, respectively, and scaled by the corresponding singular value from the diagonal of Σ. If the FROG trace is correct (the phases are correct), then there should only be one pair of vectors (one non-zero column of U and one non-zero column of V^T) and one non-zero entry in Σ. The vectors would be the E_P and E_G of the physical system.

The left and right vectors of a SVD decomposition form the "principal axes" (the principal components) of a system. At each step of the numerical recipe, if we select the left and right vector that has the largest corresponding singular value (in Σ), we can "drive" the system of solutions toward the correct (unique) pair of principal

components. From the selected pair of left and right vectors, we may form a new outer product, and rearrange the entries to again give a generated FROG trace. The phases on the entries of this new FROG trace will be different from those in the previous iteration of the algorithm, and the magnitudes will also be different. By enforcing the intensity constraint and finding a new SVD decomposition, we should find that the set of singular values begins to be "skewed" toward a larger range of values. Namely, most singular values should numerically approach zero and only one singular value remain large. A numerical tolerance may be set on the ratio between the largest singular value and the second largest singular value, and in this way the algorithm may converge. A schematic of the convergence process is shown in Fig. 3-3.

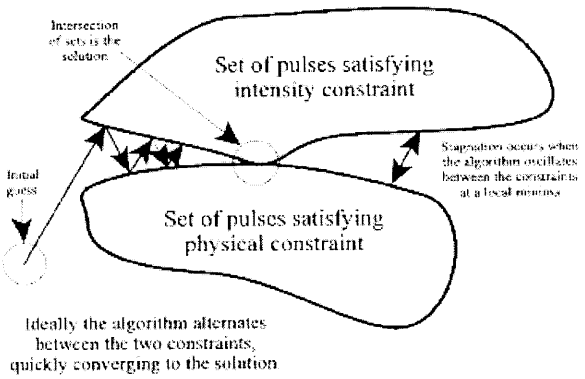

Figure 3-3: This cartoon illustrates the convergence process. The physical constraint is that the FROG trace relates to an unique pair of vectors. The intensity constraint ensures that the generated FROG trace matches the physically measured data. This figure is taken from [ ].

3.3 PCGPA and attosecond pulses

Hypothetically, we can apply the PCGPA numerical recipe to attosecond pulse characterization. Provided that experimental resolution is sufficient (delay stepping $\Delta\tau$ is small and the spectrometer can access attosecond pulse frequencies), there is no numerical reason why PCGPA is precluded from attosecond pulses. Here, we investigate

how to extend PCGPA to attosecond pulses.

3.3.1 Theoretical background

It is possible to cast the quantum mechanical dynamics in an attosecond pulse HHG experiment to produce data sets of information equivalent to those of SHG FROG for femtosecond pulses [ ]. In the literature of ultrafast pulse metrology, pulse characterization schemes that are applied to attosecond pulses are called *frequency-resolved optical gating* for the *complete reconstruction of attosecond bursts* (FROG-CRAB).

In the presence of a XUV attosecond pulse, $E_{XUV}(t)$, it is possible to photoionize neutral atoms such as Argon or Helium. If the emitted photoelectrons are in the presence of a low-frequency *dressing* field $E_L(t)$, then the quantum mechanical *transition amplitude*, under certain assumptions, may be written as the following [ ]:

$$a(v,\tau) = -i\int_{-\infty}^{\infty} dt e^{i\phi(t)}\vec{d}_{p(t)}E_{XUV}(t-\tau)e^{i(W+I_p)t} \tag{3.17}$$

$$\phi(t) = -\int_{t}^{\infty} dt'[\vec{v}\cdot\vec{A}(t') + \vec{A}^2(t')/2]. \tag{3.18}$$

Here, I_p is the ionization potential of the atom, $\vec{d}_{p(t)}$ is the dipole transition matrix, $p(t)$ is the momentum of the photoelectron $(\vec{v}+\vec{A}(t))$, W is the final kinetic energy of the electron $(\frac{v^2}{2})$, and $\vec{A}(t)$ is the vector potential of the low-frequency dressing laser field. Eq. 3.17 is qualitatively like a Fourier transform of a convolution between two signals, the "probe" $E_{XUV}(t)$ and the pure phase "gate" $e^{i\phi(t)}$. There are several assumptions that must be invoked in order for this qualitative statement to be relevant, which we will now describe.

We follow the work presented by Mairesse and Quere [ ]. The photoelectrons described by Eqs. 3.17 and 3.18 are imparted with some initial energy distribution upon ionization from a neutral atom, which is directly related to the spectrogram of the XUV pulse that ionized them. This attosecond pulse is colinear with a background, femtosecond-duration infrared pulse. The final kinetic energy distribution of the photoelectrons is dependent on their "birth time". Because the birth time is itself

a quantum mechanical parameter, the amount of "streaking" that is imparted by the IR pulse is a distribution. We assume that the femtosecond-duration IR pulse obeys the slowly varying envelope equation, so we can write

$$E_L(t) = E_0(t)\cos(\omega_L t). \tag{3.19}$$

Substituting Eq. 3.19 into Eq. 3.18, we find that [11]:

$$\phi(t) = \phi_1(t) + \phi_2(t) + \phi_3(t) \tag{3.20}$$

$$\phi_1(t) = -\int_{-\infty}^{\infty} dt U_p(t) \tag{3.21}$$

$$\phi_2(t) = \frac{\sqrt{8WU_p}}{\omega_L}\cos\theta\cos\omega_L t \tag{3.22}$$

$$\phi_3(t) = -\frac{U_p}{2\omega_L}\sin(2\omega_L t). \tag{3.23}$$

In Eqs. 3.21-3.23, $U_p(t)$ is the ponderomotive potential, equal to $E_0^2(t)/4\omega_L^2$, at the time t. θ is the observation angle between the photoelectron direction $\hat{v}$ and the laser polarization. This is typically set to 0 (on-axis). Eqs. 3.21-3.23 relate the phase of the gate function $e^{i\phi(t)}$ to the various parameters of the streaking IR field. Thus, with appropriate assumptions, we may extract information about the streaking, femtosecond IR pulse if we can determine the gate function.

Because the form of Eq. 3.17 is mathematically that of Eq. 3.2, we may use PCGPA to extract the temporal profile of the XUV pulse and the streaking IR pulse (via the approximations used in the gate function). Similar to SHG FROG for femtosecond pulses, the information of the attosecond pulse (and IR gate) is patterned onto a separate signal. Instead of a second harmonic intensity, in FROG-CRAB the information is imparted to the photoelectron energy spectrum.

3.4 Numerical simulation results

To examine the effects of PCGPA pulse characterization, we generated FROG trace data numerically in Matlab. We then fed guessed inputs to the PCGPA and compared the found solutions to the known solution. Following the theory described, it is possible to numerically create matrices of data. An example generated trace is shown in Fig. 3-4.

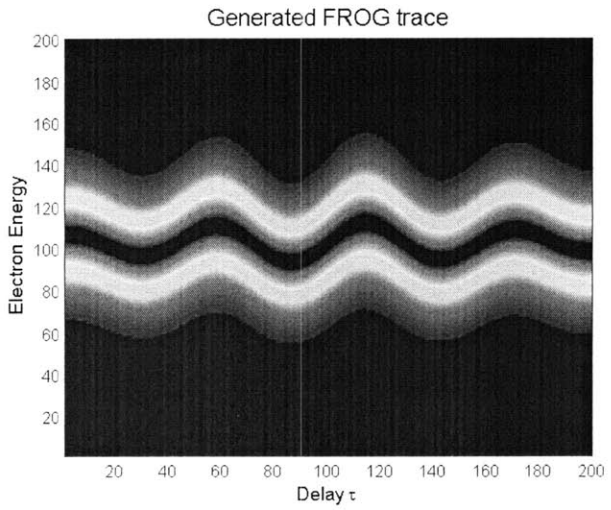

Figure 3-4: This shows the FROG trace of a generated data set. The streaking effect of the IR pulse is seen as a sinusoidal modulation of the electron energy. This occurs as the result of the short, attosecond pulse "stepping" through the (spatially) slowly-undulating IR field. The photoelectrons probe different parts of the modulated IR field.

The numerical data shows that the IR streaking field appears as an undulation in delay time τ. This is because the short attosecond pulse probes different IR field values as it slides through in delay time. A change in delay time is equivalent to a change through the spatial profile of the IR field, which is approximately sinusoidal. Thus, photoelectrons born at different delay times will see a sinusoidally-dependent IR field (as a function of τ).

Given a Gaussian-profile guess for the attosecond pulse probe vector and a sinusoidal IR field for the gate vector, PCGPA runs for several iterations and takes on the order of minutes. The numerical result is favourable and is shown in Fig. 3-5. We see

that the solved and real attosecond profiles are well within experimental tolerance. Generally, PCGPA converges well after several hundred iterations (order of minutes computation time).

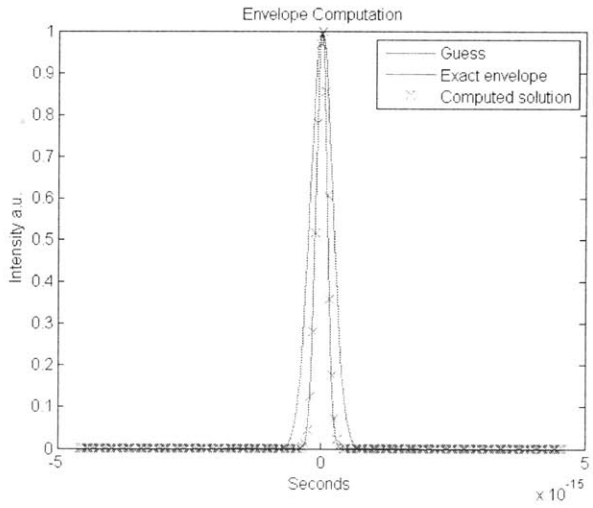

Figure 3-5: This compares the numerical result of a PCGPA to the guessed and real solutions for the attosecond-duration pulse. PCGPA is able to return an envelope that is numerically close to the real solution.

Using Eqs. 3.21-3.23, we can reconstruct the IR field profile from the solved gate function. This is shown in Fig. 3-6. By inspecting the profile of the IR field we see that we are justified in using the slowly varying envelope approximation. PCGPA is useful because it can extract both the attosecond pulse profile and the IR streaking field profile from the same data set.

3.5 Summary of Discussion

The uniqueness of the phase retrieval algorithms allows for a confident measurement of an attosecond pulse's temporal profile. These algorithms require two-dimensional data sets as inputs; the collection of the necessary data sets comprises the design goal of the experimental setup. In FROG-CRAB, the proposed method of temporal profile recovery is to use the photoelectrons to probe information about the attosecond

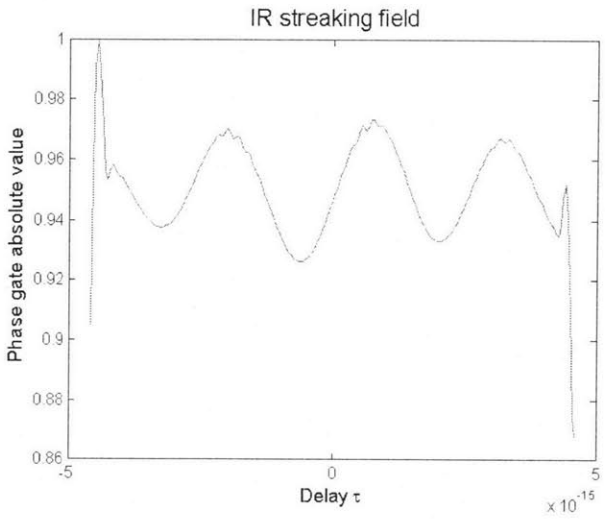

Figure 3-6: A plot of the IR streaking field as seen in the gate function $\phi(t)$. As we expect, the IR field has a slowly varying envelope.

pulse. Fundamentally, the frequency information is patterned on to the photoelectrons' energies by direct photoionization and the phase is imparted by the IR field delay. Measuring these photoelectrons accurately is the experimental challenge.

Chapter 4

Experimental High Harmonic Generation

High harmonic generation is an integral component in this thesis project. In order to understand the complete experimental setup, some details about the original system are critical. This chapter provides a brief overview of some key components in experimental HHG. Elements of the experimental HHG setup discussed in this chapter are the infrared driver pulse, the gas control system, and the spectrum measurement.

4.1 Driver Pulse

Theoretically, HHG is possible with a large variety of different wavelength ranges and pulse durations; however, there are both theoretical and practical constraints that limit the efficiency of many potential setups. Some wavelength ranges are difficult to produce with high power. The phase matching conditions of HHG also limit the range of acceptable pulses. In order to maximize the HHG output, the established system at the Optics and Quantum Electronics (OQE) group at the Research Laboratory of Electronics (RLE) uses an 800nm-centered, transform-limited femtosecond pulse (35fs) of 3 mJoule energy as the driving IR field. The 800nm-centered pulse is chosen because it is the state-of-the-art system for high-energy, femtosecond pulses. A schematic of the driver pulse generation is shown in Fig. 4-1.

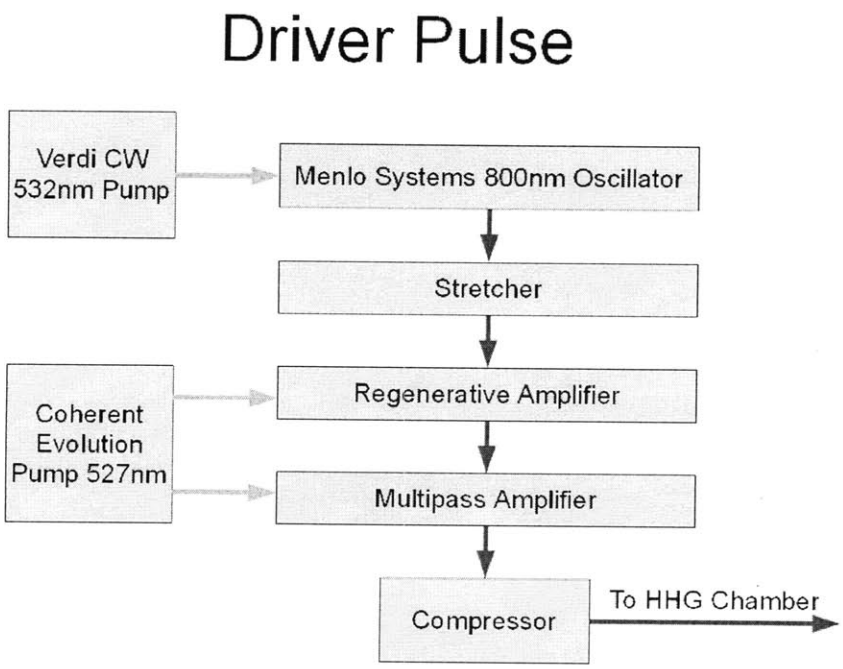

Figure 4-1: This schematic shows the main instruments and components used to generate the 800nm-centered IR driver pulse for HHG. It is possible to manipulate the pulse energy and pulse duration (compression) by tuning elements of these instruments.

The pulse begins at the oscillator stage. A Verdi-V6, continuous wave (CW) frequency doubled (1064nm) 532nm pumps a Menlo Systems oscillator. This oscillator outputs an 800nm-centered, femtosecond-duration pulse at 1kHz. The 100nm bandwidth of the pulse is Fourier transform limited to 35fs. These pulses are sent through a stretcher to separate the frequency components in time. The stretched pulse thus has a lower peak intensity, which allows the frequencies to be better amplified in the following stages.

The 800nm pulse is the seed for a regenerative amplifier and a multi-pass amplifier. These amplifiers are pumped by a Coherent Evolution-HE 527nm, 45 watt pump laser. The regenerative amplifier uses a Pockel cell to insert the seed pulse into and out of the amplification cavity. The Pockel cell is controlled by an external delay, relative to the 1kHz trigger from the oscillator, that is set by the user. The first delay controls when the Pockel cell opens to allow the seed pulse into the cavity. The second delay

controls when the Pockel cell shunts the amplified pulse out of the cavity. The final energy of the 800nm pulse varies as a function of the two delays. In order to maximize the final pulse energy, it is necessary to find the optimum delays. If the pulse is in the cavity for too short a time, it is unable to grow. If the pulse is in the cavity for too long, damage or self-phase modulation of the pulse may occur and pump energy may be lost. The 800nm pulse spectrum at the output of the multipass amplifier is shown in Fig. 4-2.

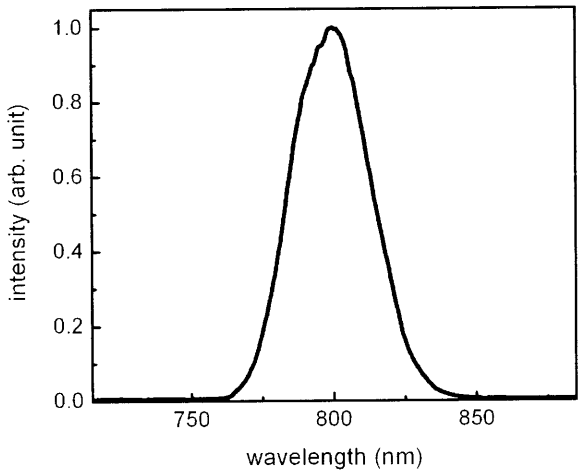

Figure 4-2: The spectrum of the 800nm pulse after the multipass amplifier. The user-controlled compressor slightly modifies this spectrum based on the external sources of dispersion throughout the optical path.

A multi-pass amplifier further amplifiers the 800nm pulse before a compressor optimizes the dispersion. The compressor is a user-tunable instrument. An optical pulse propagating through any medium, including air, is gradually dispersed. This dispersion acts primarily by imparting either net positive or net negative group delay, which is a measurement of how much and in what way the frequencies that comprise a pulse are spread in time. When the frequencies spread, the pulse duration increases, which is not desirable for a controlled experiment. In order to correct for the dispersion along an optical path, the compressor element of the driver pulse setup imparts a net dispersion that is opposite to the integrated amount over the total path. Because of the different sources of dispersion, it is impractical to numerically compute the correction; instead, an analog control is used by the experimenter to find the optimum

setting.

The typical output pulse energy is optimized at 6mJoule. This was found by using a power meter (measuring 6 watts) and the fact that the pulses are at 1kHz repetition rate. Empirically, we found that only 3mJoule pulse energy is necessary for HHG. This pulse energy is set by a rotatable waveplate in the regeneration amplifier box. Based on the angle chosen, the polarization of the 800nm pulses is altered. Before the pulses exit the amplifier system, they pass through a polarizing beamsplitter. This beamsplitter directs horizontally-polarized pulses out of the system towards the HHG setup and dumps the vertical component into an absorbing plate. Thus, by changing the angle of the waveplate, we may control the final pulse energy.

4.2 High Harmonic Generation Gas Control

4.2.1 Gas Cell

HHG occurs in a diffuse gas of nobel atoms, such as Argon or Nitrogen; thus, a vacuum system is required to evacuate a chamber for HHG. The vacuum chamber is pumped by a 350l/s turbo pump with an attached scroll (roughing) pump. This reduces the pressure inside the chamber to 5×10^{-6}mbar. HHG is possible with a pressure of $10^{-}5$mbar. Because HHG requires a nominal density of atoms to be efficient, the nobel gas must be confined to a small volume. This is done with a mechanical *gas cell*. The gas cell is a small, T-shaped assembly that has apertures for entry/exit of the optical driver pulses. The gas cell is pictured schematically in Fig. 4-3. Nobel gas is admitted into the gas cell through a pulse valve, which will be described in the next section.

The optimal gas density for HHG is not easily determined analytically, so the experimental practice is to fine tune the pressure during the actual experiment. Additionally, the notion of gas density is most often used under the assumption of equilibrium, an assumption that does not hold in an environment with an active pump. Consequently, a good experimental parameter is the gas flow into the chamber, taken

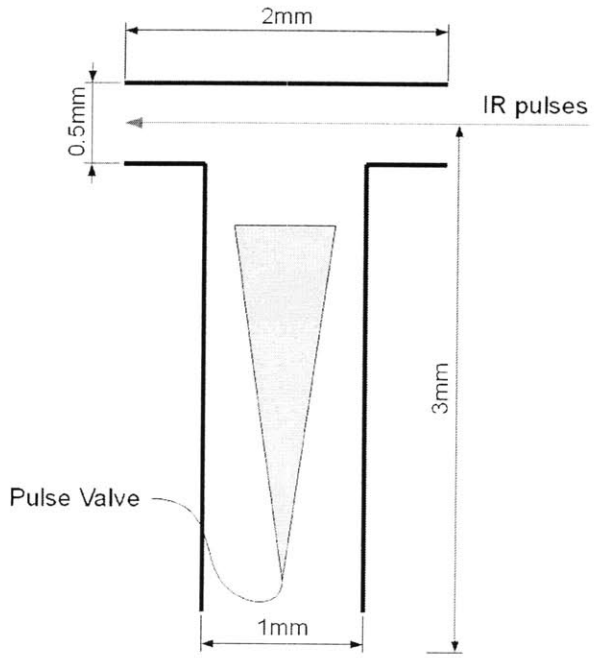

Figure 4-3: This schematic shows a cross-sectional view of the gas cell. The pulse valve admits gas into the T-shaped cell. IR pulses are focused at the center of the top cylinder. HHG occurs in this interaction region.

in standard cubic centimeters per minute (scc/m or sccm) and measured by a Sierra model Smart Trak. For HHG generation, a typical measurement of 30sccm is optimal.

4.2.2 Pulse Valve

The pulse valve has a piston-style operation and can respond at a kilohertz rate. Its action is triggered by a logic signal derived from the Menlo Systems oscillator previously described. The exact behaviour of the pulse valve is determined by a control signal that is generated from the trigger. In particular, the voltage and the width of the control signal set how much the valve opens and for what duration, respectively. In the HHG setup, only fifty of the one thousand trigger signals per second are used. The total duration of these fifty signals is 50ms because the Coherent regenerative amplifier has a 1kHz repetition rate. This choice was made to control the gas flux into the HHG vacuum chamber. If each optical pulse was used, it would necessitate one thousand openings/closings of the pulse valve, which empirically were shown to increase the vacuum chamber pressure too much.

The control signal for the fifty pulses is a logic train of square waves. The control signal is sent to a high voltage power supply (x10 gain), which is directly connected to the pulse valve by a BNC cable and vacuum hardware feedthrough. The pulse valve is capable of voltages between 0 and -350 volts, so the maximum amplitude of the control signals is -3.5 volts.

The user has three variables under control: the delay between optical pulse trigger and pulse valve signal, the duration of the square waves (duty cycle), and the amplitude of the square waves. Fig. 4-4 shows a schematic of the control signal and the user-controllable parameters. The delay between optical trigger and the pulse valve control signal sets the delay time before the pulse valve opens. There is a natural lag time for the gas to expand into the small gas cell. The user is able to adjust for an optimum delay so that the gas has enough time to distribute well within the cell before the IR driver pulse enters the chamber. Because the optical pulses have 1kHz repetition rate, the maximum theoretical delay is one millisecond; however, a typical experimental delay is closer to 0.5ms.

The width (duration) of the square wave sets the duty cycle of the pulse valve, which is the ratio of the width of the square wave to the cycle period. The width of the square wave determines the duration for which the pulse valve is open, which in turn relates to the amount of gas admitted into the gas cell. This is an important parameter because the gas density affects HHG phase matching (efficiency). A width of 0.5ms would be a duty cycle of $\frac{0.5ms}{1ms} = 50\%$ because the repetition rate of the driver pulses is 1kHz. The empirically-determined optimal width is about 0.1ms (10% duty cycle).

Finally, the amplitude of the square waves may be set by the user. The amplitude determines how much the piston-style pulse valve opens (piston head displacement). The gas flow rate into the cell is a function of how much the valve opens. This parameter is different from the square wave width because the flow rate controls the instantaneous density/pressure in the cell. During an HHG experiment, the amplitude is set to the maximum (-3.5 volts), which was found to result in the best HHG efficiency. For other applications, it may become necessary to control the pulse valve

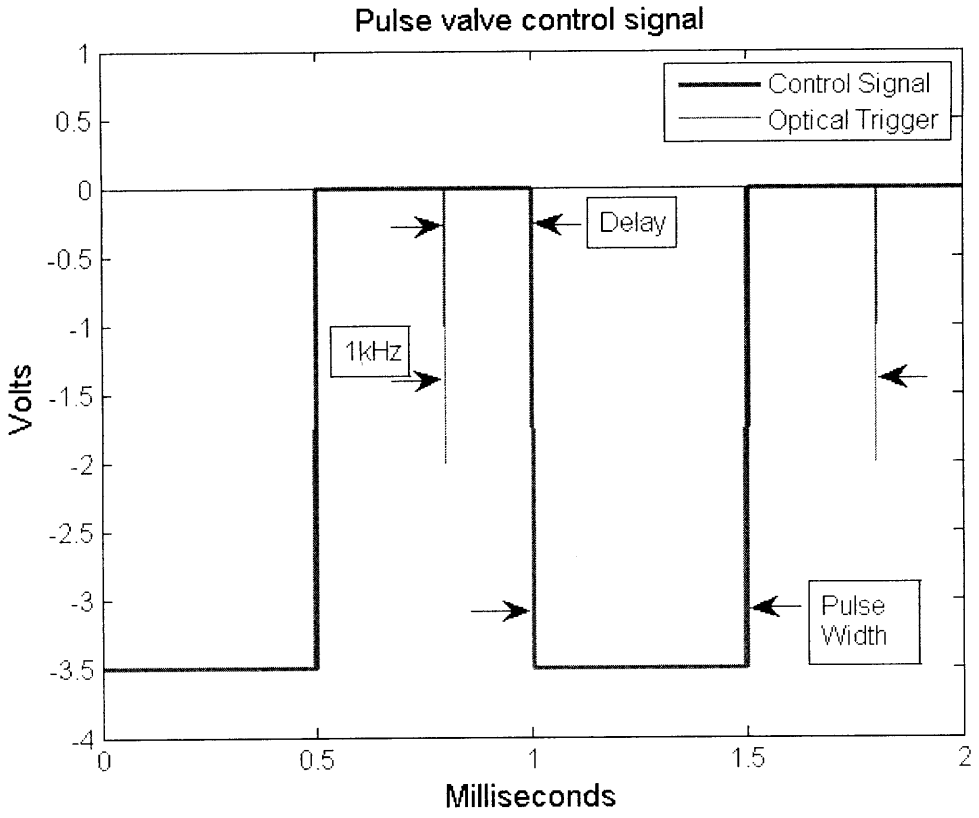

Figure 4-4: One cycle of the fifty-cycle pulse valve control signal is shown. Once per second, the train of fifty square waves activates the pulse valve. This schematic shows the width and delay, both user-controllable parameters. The amplitude is set to -3.5 volts, as is typical for our HHG system, although the amplitude is also a tunable parameter. The IR driver signal ("optical trigger") has a 1kHz repetition rate; thus, the trigger is separated by 1ms. It is seen that if either the square wave width or the delay exceeds 1ms, the control signal will alias into the following optical pulse.

opening.

4.3 Measuring XUV Spectrum

Inside the gas cell, the IR driver pulse interacts with gas' atoms to generate XUV radiation. This XUV is coherent and composed of higher harmonics of the IR femtosecond pulse, as described in the chapter on HHG theory. The XUV and IR pulses exit the gas cell co-linearly. At this stage in the optical path, the co-linear pulses travel without significant dispersion (vacuum has a flat index of refraction). In order

to measure the spectrum of only the attosecond XUV pulse, the IR femtosecond pulse must be filtered. This is achieved by a thin (100nm) film of aluminum. Aluminum filters IR frequencies and attenuates the XUV by 50%. Different filters are available of various materials and thicknesses.

After the IR is filtered, the XUV beam may be studied. The spectrum is obtained with a spectrometer calibrated specifically for the XUV bandwidth. The XUV beam strikes a grating, which Bragg reflects the different frequency components at different angles; thus, the frequency information of the attosecond pulse is patterned onto the angular spread of the XUV frequencies. The grating is interchangeable, and serves as the method for matching the spectrometer to different frequency ranges.

Chapter 5

Design Goals

This chapter enumerates and explains the various design goals and challenges of the FROG-CRAB apparatus constructed. In the chapter about the numerical phase retrieval algorithms, we learned that the input into the algorithms is a two-dimensional set of data. The two parameters of interest are the photoelectron energy and the delay between the attosecond pulse and the IR streaking field. These parameters are used because the quantum mechanical effect of streaking photoelectrons with an IR field reproduces the FROG trace data. Resolving the photoelectron energy spectrum and timing delay between attosecond and IR pulses is a multi-variable challenge that entails issues such as stability, control precision, optical power, and data management. We explore these considerations before discussing the experimental implementation of our conclusions.

To motivate the experimental setup, we first review the various design considerations that were explored. A general list of design goals is as follows. The items are organized as they would occur in an actual experiment. Note that the design of the experiment accounts for all aspects of measurement, stability, and control.

Vacuum Chambers: Maintaining the required operating pressures.

Streaking Field: An optical pulse used to streak the energy spectrum of photoelectrons emitted from atoms ionized by XUV pulses.

Pulse Overlap Detection: A rough temporal alignment of the attosecond XUV and IR streaking pulses.

Temporal Stability: A system to maintain temporal stability by filtering external vibrations in the experiment.

Timing Delay: The time delay between the attosecond pulse and IR streaking field.

Optical Focusing: A system to capture the most XUV power in the interaction region.

Spatial Recombination: A system to combine the attosecond and IR streaking pulses into a co-linear propagation.

Gas Inlet: Finding the correct amount of gas to admit into the interaction region for photoelectron emission.

Time-of-flight Spectrometer: An instrument designed to measure particle energies to be used to gather data on the photoelectron spectrum.

Data Acquisition and Management: The computer setup for acquiring and storing data and for managing the automated elements of the experiment.

5.1 Vacuum Chambers

There are three main reasons for using a vacuum in this experiment. The intense optical pulses used in both HHG and FROG-CRAB experiments readily ionize air molecules. A vacuum system removes the effects of plasma radiation from ionized air. Additionally, there is no absorption in a vacuum, which is important for maintaining the attosecond XUV pulses throughout the optical path. Finally, by allowing a gas to enter the vacuum chambers at the interaction regions of HHG and FROG-CRAB, the experimenter can chose both the type of gas and the optical properties that depend on the gas parameters.

Femtosecond pulses of 3mJoule energy easily ionize air molecules. This effect has been discussed in previous chapters about HHG. From the standpoint of FROG-CRAB, the measurement of photoelectron energies needs to be normalized to a known property; namely, the atoms that release photoelectrons by absorption of XUV radiation must all be the same element. If the atoms were different elements, then the photoelectron spectrum would contain information about different ionization potentials. The different ionization potentials would contaminate the data because FROG-CRAB relies on using an IR field to streak the photoelectron energies. Different ionization potentials may be indistinguishable from IR streaking.

XUV radiation is readily absorbed in most mediums, including air. The vacuum system maintains a low enough pressure for XUV absorption to be minimal. Additionally, the lack of dispersion management such as an XUV compressor stage means that dispersion along the optical path would have an adverse effect on the profile of attosecond pulses. Although XUV absorption by air is a more important issue, a vacuum system would address any potential pulse broadening by dispersion because a vacuum is non-dispersive.

Gas type, density, and volume all have important affects on the efficiency of HHG (phase matching) and the results of FROG-CRAB. Just as a vacuum removes the problems of ionizing many different kinds of atoms and molecules found in air, a vacuum allows the experimenter to find the optimum balance of flow rate and gas type for FROG-CRAB.

5.2 Streaking Field

FROG-CRAB uses a separate optical field to streak the energy spectrum of the photoelectrons emitted from atoms ionized by the attosecond pulse. A photoelectron energy spectrum cannot be acquired with only one attosecond ionization event. Multiple ionization events (experimental "shots") are required. Thus, over the course of the FROG-CRAB experiment, the streaking field needs to be in phase with the attosecond pulses. If the streaking field shifts in phase between shots, the photoelec-

trons will probe different amplitudes of the streaking field.

In the chapter on HHG theory, we learned that the IR femtosecond field imparts its phase to the generated attosecond pulses. A natural choice for a streaking field is to use part of the actual IR driver field. Assuming perfect stability, this will ensure that the attosecond and streaking pulses have the same relative phase shot after shot. An experimental setup that splits part of the driver IR field before HHG will allow us to use the femtosecond pulse as the streaking field.

5.3 Pulse Overlap Detection

FROG-CRAB works by streaking an IR field on photoelectrons emitted by atoms that ionize due to the attosecond pulse. The IR streaking can only occur if the femtosecond pulse is co-linear and temporally overlapped with the attosecond pulse. The femtosecond pulse used in FROG-CRAB is 35fs in duration, which corresponds to 10 microns. The attosecond pulses are on the order of thirty times smaller; thus, the overlap between IR and XUV has effectively ten microns of tolerance. A system to detect this temporal overlap needs to be standardized for FROG-CRAB experiments.

5.4 Temporal Stability

Stability on the nanometer scale is important for this FROG-CRAB experiment. The attosecond and streaking pulses take different paths before being combined. Once overlapped, the optical path is that both pulses take should be equal (the net path difference is zero). If the path difference fluctuates due to external vibrations, the two pulses will slip in phase relative to each other. A displacement on the order of several hundred nanometers will be easily detectable on the photoelectron spectrum because the photoelectrons probe a different amplitude of the streaking field. A feedback-controlled mechanical stabilization setup will reduce the statistical errors due to external vibrations.

5.5 Timing Delay

The timing delay between the attosecond pulse and IR streaking field needs to be controlled in addition to be accurately measured. FROG-CRAB numerical algorithms require that the streaking effect on the photoelectron energies has a smooth functional dependence on timing delay. Thus, the delay cannot have large step sizes between photoelectron energy spectrum measurements. To calculate an appropriate delay step size, an estimate is to consider the IR streaking field as a continuous wave at 800nm wavelength. The attosecond pulse is very short in time relative to one cycle of the IR streaking field so it effectively "probes" the instantaneous IR field at each respective delay step. The Nyquist sampling rate for the 800nm continuous wave requires that the attosecond pulse experiences discreet delay steps that translate no more than 400nm. For a smooth exploration of the IR streaking field, the delay steps should be on the order of 100nm. This condition enforces a stability and controllability limits on any delay-stepping system.

5.6 Optical Focusing

XUV radiation from HHG diverges from the interaction region (gas cell) as a typical Gaussian beam. The photoelectrons used for FROG-CRAB are generated by ionizing atoms with the XUV radiation. This process is most efficient if the XUV is focused on the interaction region. Normal optics (lenses and spherical mirrors) absorb strongly in the XUV wavelength range. Part of the FROG-CRAB setup needs to use optical elements that are capable of focusing in the XUV wavelength range.

The IR streaking field should also be focused at the interaction region for efficiency. Choosing an appropriate focal length for the IR is important. When Gaussian beams are focused, the light undergoes a phase shift known as the Gouy phase. Along the propagation direction $\hat{z}$, a Gaussian beam experiences a phase shift of

$$\phi(z) = \arctan\left(\frac{z}{z_R}\right) \tag{5.1}$$

where z_R is the Rayleigh range, which is a property of each Gaussian beam. Qualitatively, the Gaussian beam acquires a π phase increase going through a focus. The rate of phase increase is related to how tightly the beam is focused. This Gouy phase may be important in the context of FROG-CRAB because the actual interaction region between the gas and the attosecond and streaking pulses has some spatial volume. The phase of the streaking field is imparted to the photoelectrons. If the streaking field has a phase that changes quickly over the interaction region, the photoelectron spectrum may be broadened. This is a qualitative argument that is addressed experimentally.

5.7 Spatial Recombination

We have chosen to use part of the IR driver pulse as the streaking field. This streaking field is split from the main driver pulse by an optical element and must be recombined with the attosecond pulses after HHG. For FROG-CRAB, the optimum geometry has the attosecond and streaking pulses aligned co-linearly. A technique for combining the two pulses must be included in the experimental setup. Note that this combination may only be done after the driver IR pulse, which created the attosecond pulses via HHG, is filtered by the aluminum film.

5.8 Gas Inlet

The experimenter should control the type and amount of gas that is ionized by the attosecond pulse. This is done by using a gas jet with a needle aperture inside the vacuum chamber. Positioning the gas jet and balancing the gas flow rate are both methods of control that the experimenter has to optimize the setup. Gas flow into a vacuum is a complicated problem that may be solved with numerical simulations; however, typically there may be uncontrollable influences that cause turbulent flow or other difficult to treat effects. The difficulty of easily obtaining an analytically-optimum geometric configuration implies that an experimental approach is the best.

Testing different configurations of gas nozzles, flow rates, and positions is an integral part of the FROG-CRAB apparatus.

5.9 Time-of-flight Spectrometer

A time-of-flight spectrometer (TOF) is an instrument that is used to measure the time it takes a charged particle to traverse a field-free tube of known length [12]. Because electromagnetic fields are screened, charged particles do not experience accelerations. Thus, if the time that an electron enters this tube is known, then the measured time it took the electron to fly the length of the tube can be used to calculate the electron's kinetic energy. For example, if it takes t seconds for an electron to traverse a tube of length L, then the electron's kinetic energy is calculated as:

$$v = \frac{L}{t} \tag{5.2}$$

$$E_k = \frac{1}{2}mv^2 = \frac{mL^2}{2t^2} \tag{5.3}$$

where v is the electron's (constant) velocity and E_k is the calculated kinetic energy. For the photoelectron energies expected in the FROG-CRAB experiment, classical dynamics apply (instead of relativistic dynamics).

In Eq. 5.3 we see that the only experimentally-measured parameter is the time of flight, t. A TOF instrument alone does not record the time of flight. In practice, a sophisticated electronic component is used to record both the time a photoelectron enters the field-free TOF drift tube and the time the photoelectron crosses the entire length. This setup will be described in more detail in a following chapter; for the purposes of motivating an experimental design we see that the TOF equipment must be accounted for.

5.10 Data Acquisition and Management

The FROG-CRAB experiment needs a large, two-dimensional dataset in order to retrieve the temporal profile of an attosecond pulse. Such a dataset requires many photoelectron shots. At 1kHz repetition rate for pulses (shots), a typical experiment may take several hours to assemble a complete dataset. Additionally, the timing delay control should be automated. Thus, in practice, the experiment needs to be automated by computer software as much as possible. Using a computer to control the experiment is also preferable because the numerical algorithms used for phase retrieval are a fundamental component of FROG-CRAB.

Chapter 6

Time-of-flight Spectrometer System

In this chapter, I explain the time-of-flight spectrometer (TOF) system and operation. This includes a description of the mechanical design of the TOF drift tube, the signal output of the multichannel plate (MCP), and the electronic recording card. The process for obtaining the photoelectron spectrum is described. This TOF system is explained out of context of its physical placement within the larger FROG-CRAB experimental setup. The information about its final location will be discussed in a following chapter on the experimental layout. Please refer to Fig. A-1 located in the Appendix for a schematic of the TOF instrument.

6.1 TOF Design

The main body of a TOF is a 35cm tube (called a "drift tube") that is shielded to keep the interior region free of any external electromagnetic fields. This is done by using a high mu-metal sheath and carefully grounding the surrounding components. The interior of the drift tube can be kept ideally field-free so that charged particles do not experience acceleration when inside. This means that if a photoelectron ionized by the attosecond pulse enters the drift tube, it will continue on a linear trajectory until it strikes a barrier such as a wall or the back of the TOF. Photoelectrons that strike

the interior walls of the drift tube represent lost data because the actual measurement device, called a multichannel plate, is located at the back of the drift tube. Thus, the TOF is designed so that photoelectrons that enter the drift tube have a clear trajectory only to the MCP at the back. The entire TOF assembly attaches to the side of a vacuum chamber by a six inch connection flange (seen in Fig. A-1) at the back of the drift tube.

Confining the photoelectron trajectories is accomplished by two methods. The first method is to limit the acceptance angle into the drift tube. The "focus" of the TOF is 3mm from the tip of the drift tube. At this location, a cross section of 200 microns defines a small volume from which emitted photoelectrons have a clear trajectory into the drift tube. As viewed from the center of this interaction region, the acceptance cone of the TOF nozzle is only 6 degrees (full angle). A negative consequence of this limited acceptance solid angle is that only about 0.1% of isotropically-emitted photoelectrons are captured by the tip of the drift tube.

To increase the acceptance angle of the TOF, the photoelectrons that enter through the TOF aperture are geometrically aimed at the back MCP by an electrostatic "lens" [ ]. The lens is located at the front of the drift tube (called "extraction optics" in Fig. A-1) and consists of plates that may be charged by a high voltage power supply. When configured properly, the electrostatic lens can increase the acceptance cone to 45 degrees full angle, which is 3.8 % of the full 4π steradians. The voltage is set by the user and optimized based on real-time measurements using an oscilloscope (a process that will be detailed) but is nominally five times the photoelectron kinetic energy (30eV 150V on the lens). The lens works by using electrostatic fields to bend the photoelectron trajectories that would otherwise strike the inner wall of the drift tube. Although it is possible to operate the TOF without the electrostatic lens, optimizing for the correct voltage can dramatically increase the capture rate per second.

In addition to screening external electromagnetic fields, the TOF drift tube requires a vacuum in order to prevent the photoelectrons from colliding with air molecules. The TOF is equipped with a six inch flange at the back near the MCP. The MCP also requires a vacuum to prevent breakdown, which will be explained. In practice, the

TOF is pumped by an Edwards nEXT 300D model attached to the six inch flange. This model is capable of of 250l/s pump rate. An Edwards scroll pump is used as a backing pump for the turbo pump. The pumps connected to the chamber at the front end of the TOF also helps to keep the pressure low inside the drift tube, which acts as a differential vacuum stage.

The TOF is also equipped with additional electrostatic lenses inside the drift tube that can be used to either slow or accelerate charged particles. This feature is used to change the energy range detectable by the TOF and accompanying electronics. If an accelerating voltage is applied, low-energy, slow photoelectrons will reach the MCP in a shorter amount of time than in a truly field-free drift tube. The converse is true in which fast electrons can be slowed by a retarding voltage. Although it is necessary to calibrate for this time offset, this feature allows the TOF to probe photoelectrons of very high to very slow velocities.

6.2 Multichannel Plate

The MCP is an advanced tool that can detect individual charged particles [ ]. A MCP is a plate with densely-packed, small channels embedded in the material. A high voltage of up to 2kV is applied to these channels. When a charged particle strikes a channel, the high voltage causes a cascade of electrons to flood down the channel. On the back side of the MCP the electrons are captured by an anode plate, which records the current spike as a voltage signal. The actual channels are made in a "chevron" formation [ ]. Looking at a side-on cross section, each channel is tilted, as seen in Fig. 6-1. A thin gap exists between oppositely-tilted channels. The initial electron cascade from the top layer of channels spreads in the gap into neighboring channels, which helps to generate a larger signal on the anode plate. The chevron design also helps to reduce ion feedback, in which stray ions may travel the length of a channel to create a false signal.

The MCP used in our TOF must operate at a pressure of no more than 8×10^{-6}mbar. A lower pressure is preferable. MCPs in general have a pressure limit

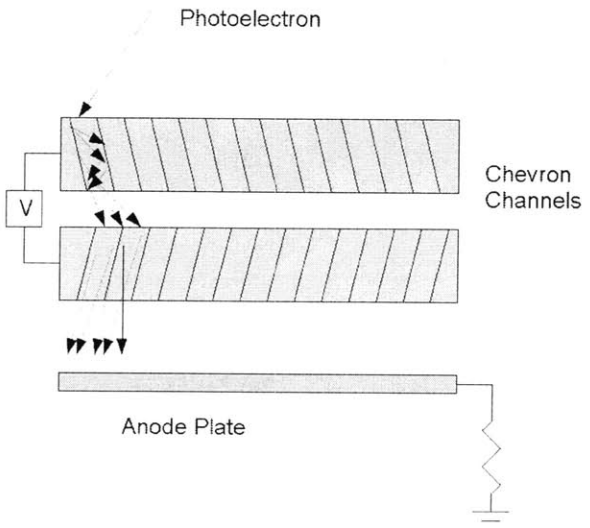

Figure 6-1: A cross sectional schematic of a MCP with chevron channels. A single charged particle can cause a cascade of electrons that are recorded as a voltage signal.

because the high voltage across the channels may cause arcing if too much gas is present. This is an additional reason for the pump assembly to be attached at the back of the TOF (near the MCP).

The voltage signal output from the MCP is in the range of -10mV. This signal is sent through a BNC cable to a 4GHz preamplifier stage with sixteen times gain, which increases the amplitude of the final signal to about -150mV. Each time a photoelectron strikes the MCP, this voltage signal is used to record the flight time.

6.3 Electronic Recording

The output of the TOF is a voltage signal from the MCP. This voltage signal corresponds to a photoelectron striking the MCP. In order to extract a kinetic energy for the photoelectron, this voltage signal must be related to a time of flight through the drift tube. This implies that we must have a reliable method for determining the time when a photoelectron first entered the drift tube. To understand what kind of electronics are necessary for the timing and recording of the TOF signals, we evaluate a simple example.

The timescale of the data is set by a few different experimental parameters. As an

estimate for how long it takes a photoelectron to travel the 35cm length drift tube, consider the ionization of an Argon atom by a 50eV XUV photon. The ionization potential of Argon is about 15eV. An emitted photoelectron may have up to 35eV of kinetic energy. To calculate the time of flight, we use the following equation:

$$t_{\mathrm{TOF}} = \sqrt{\frac{mL^2}{2E_K}} \tag{6.1}$$

where m is the electron mass, L is the length of travel (drift tube length), and E_K is the kinetic energy. Using the relevant numbers, we find that

$$t_{\mathrm{TOF}} = \sqrt{\frac{\frac{0.511\mathrm{eV}}{c^2} \times (35\mathrm{cm})^2}{2 \times 35\mathrm{eV}}} \approx 100\mathrm{ns}. \tag{6.2}$$

A typical photoelectron from our FROG-CRAB experiment will traverse the drift tube in a time on the order of one hundred nanoseconds. Resolving signals on the order of one hundred nanoseconds is possible with electronics that operate on the megahertz scale; however, differences in photoelectron energies may be on the order of one eV, not tens. The rate of change of kinetic energy as a function of time of flight may be calculated:

$$\Delta E_K \sim \frac{mL^2 \Delta t}{t_{\mathrm{TOF}}^3}. \tag{6.3}$$

Using Eq. 6.3, a photoelectron time of flight of 99ns versus 100ns (Δt = 1ns) amounts to nearly one eV of kinetic energy difference (using t_{TOF} = 100ns). We want to have experimental resolution on the order of one eV, so would necessitate electronics that are on the GHz scale. Such electronics are specialized and state-of-the-art.

Multi-channel analyzers (MCA) are data acquisition cards designed to record the time a voltage signal is received. Typically, MCAs have a high time resolution. They work by discretizing time into a vector of time bins. Experimental data consists of a string of numbers, each corresponding to one time bin. MCAs only record when a predetermined falling-edge voltage is measured. This trigger is called a "stop

event". A number is placed in the appropriate time bin to reflect this information. It is important to note that MCAs can record at most only one stop event per time bin. Thus, if two photoelectrons coincide perfectly in time, the MCP voltage signal will be higher in amplitude (a larger current from two photoelectrons); however, the MCA will only record a single stop event. This is a design constraint that must be used to balance the rate of photoelectron captures by the TOF. In particular, for each attosecond pulse (each experimental "shot"), we optimize to expect only one photoelectron measurement on the MCP in order to not confound the data.

In our FROG-CRAB setup, we use a MCA model P7887 from the company Fast ComTec. This MCA is capable of a 250 picosecond time bin discretization (4 GHz sample rate). There are several options available for operating the MCA, the most important of which is the "acquisition delay". The card starts counting when a "start event" is triggered by a user-determined voltage setting. The user has the option to have the card not search for events for some time, which is called an "acquisition delay". This is useful to conserve memory space instead of recording data which is known to have no photoelectron counts. In the experimental setup, the "start event" is the oscillator 1kHz signal sent to the HHG system. There is a delay due to electronic and physical processes in the experiment, between the oscillator signal and the actual FROG-CRAB attosecond pulse ionization event in the TOF interaction region. Determining the appropriate timing for the MCA card is discussed below.

When the MCA is actively seeking events, it steps through as many time bins as the user wants. For each time bin, the MCA records a "0" for no event and a "1" for a stop event. A scan across the user-set time bin window is called a "sweep". In a sweep there may be multiple stop events; however, because a stop event is triggered by a falling edge voltage signal, the MCA is unable to measure the amplitude of the signal either within one time bin or across several. A two-photoelectron signal would be proportionally stronger than one photoelectron, but the result on the MCA would only be a "1" for the coincident time bin. The limitation of being unable to measure MCP signal's amplitude constrains the experiment. The photoelectron energy spectrum has a distribution where some energies have a higher probability.

Thus, if two photoelectrons with nearly the same energy are released, their time of flight may be within 1ns (corresponding to 1eV of difference). The MCA will only register one event at the related time bin, although physically two photoelectrons were present. This represents lost data, which will artificially flatten the photoelectron spectrum. To avoid this effect, the experiment must be tuned such that only one photoelectron on average is captured per attosecond pulse (per experimental shot).

The P7887 MCA card has an attached software package. This package contains a user interface and a network server. The user interface can control all functions of the card and save datasets. From the standpoint of automation, the best option is to use the server. The P7887 MCA is programmed to respond to a list of commands that are sent to the server. It is possible to send commands to the MCA via the server by using Matlab. By saving a command as a string in Matlab, we can call the server and pass the string as a command. The advantage of using Matlab is that a hierarchy for controlling the entire experiment is implementable. Controlling the P7887 MCA's data acquisition and storage is a subroutine within the larger structure of the experiment.

6.4 Initialization of TOF System

This section describes the standard protocol for starting the TOF system, which includes the vacuum environment, the TOF instrument, and the P7887 MCA card and software. In this description, we assume that Argon is being used for FROG-CRAB.

After establishing HHG in the setup (which will be discussed in the future chapter), we start to allow gas to flow into the vacuum chamber where the attosecond and streaking interaction takes place. The gas inlet is positioned on one of the axis of the interaction region. The other two axes are the co-linear attosecond/IR pulse propagation direction and the TOF drift tube nozzle. The gas that flows into this interaction region should be optimally positioned such that most of the expanding gas may interact with the pulses. This will minimize the required gas flux into the

vacuum, which helps to keep the pressure low inside the TOF.

On startup, we use the Sierra model Smart Trak 2 flow controller to set the gas flow at 0.5 scc/m. Keeping the TOF high voltage supply off, we use the hot filament pressure gauges to check the pressure in both the TOF vacuum chamber and inside the TOF near the MCP. With the Edwards 250l/s turbo attached to the TOF, we are able to maintain a pressure inside the TOF that is ten times lower than the pressure in the vacuum chamber. The threshold safe TOF vacuum pressure is 8×10^{-6}mbar. At 0.5 scc/m, the turbo pumps are able to maintain a pressure lower than the threshold. 0.5 scc/m is a typical flow rate but this value may be changed depending on other experimental conditions. With a high attosecond pulse energy, more photons are available per shot so the gas flow may be increased. For a low pulse energy, a lower gas flow is used. In either scenario, the goal is to obtain one MCP event per shot, or fifty counts per second (remembering that HHG is only active for fifty of the one thousand pulses per second). This can be checked with an oscilloscope, which will be described later.

The gauges are used to check for this before turning on the TOF. Because the hot filament gauges work by heating a cathode, stray electrons are present in the local environment. The gauge on the TOF near the MCP must be switched off prior to turning on the high voltage power supply. The gauge emits enough stray electrons to saturate the MCP because of its close proximity. Switching the hot filament gauge off ensures that the MCP is protected.

The high voltage power supply is slowly increased to 1kV, allowed to come to equilibrium for thirty seconds, and then raised to about 1.75kV. The MCP operates normally at this voltage. It is possible to increase the voltage up to 2kV, but this is unnecessary and risks damaging the MCP by arcing. At this point, the gas is flowing into the interaction region and the TOF high voltage supply is on.

As described in the chapter about the HHG experiment, for each second only fifty of the 1kHz repetition rate pulses are used. This is to reduce the gas load in the HHG vacuum chamber. To obtain the 1kHz train of fifty pulses, computer software is used to generate a logic signal that is sent through an AND gate with the oscillator 1kHz

continuous waveform. We want the P7887 MCA to look for photoelectron signals only when the attosecond pulses are being generated in this fifty millisecond window. If the MCA is continuously looking for signals, the likelihood of reading stray ions or false signals increases, which introduces a larger statistical error in the data. We will use the train of fifty 1kHz logic pulses as the basis for controlling the MCA.

Prior to connecting the MCP output to the P7887 MCA, we use an oscilloscope to check for photoelectron detection and for determining the "start event", "stop event", and "acquisition delay" settings for the MCA. For the start event, the parameter that must be determined is the falling edge trigger voltage. The P7887 only triggers a start and stop event on a falling edge. We use the oscillator 1Khz pulse signal, which is a train of short square waves, as the start event triggers for the MCA. The P7887 can only accept voltages that are between ± 1.7V. Thus, it may be necessary to attenuate the oscillator 1kHz signal with power attenuators to be within tolerance. We trigger the oscilloscope from the fifty 1kHz logic pulses and observe their shapes. We expect to see a sequence of fifty short square waves that are separated by 1ms, which corresponds to the 1kHz repetition rate of the oscillator. Note that the P7887 only triggers on a falling edge, so when setting the start event voltage value it is important to note that the rest of the experimental setup uses the *rising* edge as a trigger. This fact is used when calibrating the time of flight data to an absolute metric.

Once a start event trigger voltage has been set, the stop event and acquisition delay settings may be determined. If the gas flow is chosen well, the TOF aligned with the interaction region, and the attosecond pulse energy sufficiently large, we expect to see at least one photoelectron detection per oscilloscope trigger. On an oscilloscope, this will appear as a *negative* voltage spike that comes after the rising edge of the 1kHz logic pulse. Ideally, we want the stop event trigger voltage to be the most negative possible in order to screen out random fluctuations on the MCP. If the stop event voltage is set too low, no events will be recorded because the photoelectron MCP signals have an empirical maximum amplitude. Typically, we use -150mV as stop event voltage.

Qualitatively, the acquisition delay represents the "dead time" between the 1kHz logic pulse and the true photoelectron emission event in the TOF interaction region. This dead time is due to electronic delays through cables and the propagation of light throughout the experiment. Although the electronic and optical propagation delays may seem trivially short, a signal traveling at the speed of light takes 3ns to travel one meter. Considering the several meters of integrated propagation distance in the experiment, a delay of tens of nanoseconds is expected. Determining the exact delay is difficult to do by measuring distances. In practice, the best technique is to intelligently estimate a value close to the actual delay and later to compare a flat (without streaking field) photoelectron spectrum to the XUV spectrum as found with the spectrometer. The photoelectron spectrum should be linearly related to the XUV spectrum, according to FROG-CRAB theory. Factored into the acquisition delay is the estimated dead time due to the photoelectrons traveling through the drift tube. For a photoelectron of 35eV kinetic energy, we calculated a nearly 100ns time of flight for the 35cm drift tube. It is unnecessary for the MCA to be active during the flight time. If a retarding or accelerating field is applied within the drift tube, an appropriate acquisition delay must be determined.

In the automated FROG-CRAB experiment, the master Matlab program controls the data acquisition and storage from the P7887 MCA. The P7887 software is commanded to store sweeps as ASCII text files that can be accessed by Matlab easily. Matlab also sets the start, stop, acquisition delay, and maximum number of time bins for each sweep. The experimenter, in turn, can augment any of the parameters as desired by changing the appropriate commands directly in Matlab to avoid using the P7887 interface software package. An example of TOF data is shown in Fig. 6-2.

Matlab allows the MCA to collect the photoelectron spectrum for a single delay step. At a rate of fifty events per second, with several hundred possible time bins, acquiring a statistically-reliable histogram of flight times will take many minutes. During this time, stability is crucial for keeping the statistical noise at a minimum. This will be discussed in a following chapter. Once the histogram is complete, the timing delay between attosecond and IR streaking pulses is advanced, and the next

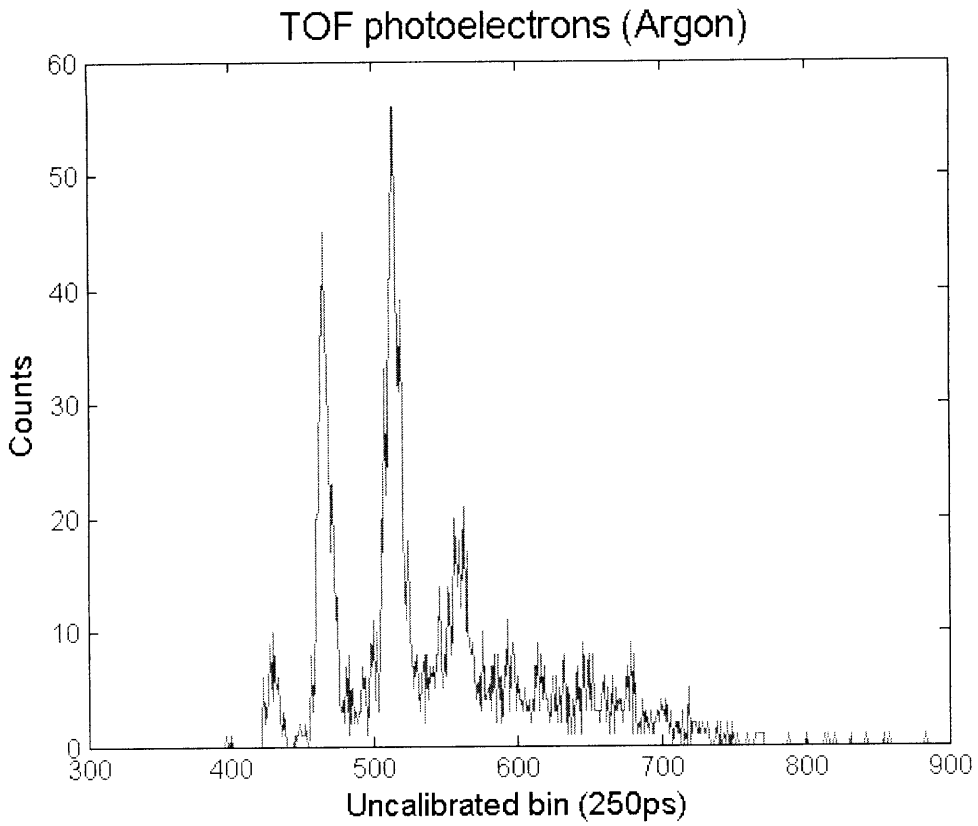

Figure 6-2: This plot shows uncalibrated photoelectron counts as a function of time bin. When calibrated, each time bin will correspond to a photoelectron kinetic energy. This final calibration is best performed by comparing a flat photoelectron spectrum to the XUV spectrum from the spectrometer. The distinct peaks are representative of the features seen on a spectrum of a pulse train, which shows that the spectrum from the attosecond pulse train is patterned onto the photoelectrons.

photoelectron spectrum is collected. In this way, the two-dimension dataset is accumulated over many delay steps.

6.5 TOF Limitations

The TOF has two sources of bandwidth limitation. The physical length of the drift tube (35cm) constrains how fast the photoelectrons can travel and still be resolvable. At 200eV kinetic energy, a photoelectron will traverse the drift tube in about 40ns. For a 1ns difference in time of flight at this energy range, the energy dispersion in Eq. 6.3 is 11eV. Each time bin (250ps) corresponds to nearly 3eV of kinetic energy

difference. Our energy resolution is considerably worse than at timescales of 100ns, for which one time bin is about 0.25eV. The loss of energy resolution limits the TOF to photoelectrons with a kinetic energy typically less than 200eV. To access photoelectrons with higher kinetic energy, it is possible to use the electrostatic plates inside the drift tube to slow down photoelectrons to energies less than 200eV.

The second source of bandwidth limitation is due to the electrostatic lens used to direct photoelectrons towards the MCP. The lens is designed to operate at a voltage that is five times the kinetic energy of the photoelectrons (30eV 150V on the lens). When the photoelectron energy spectrum is broad, it is only possible to properly optimize the lens' voltage for one kinetic energy. This creates a chromatic aberration effect, in which photoelectron kinetic energies that the focusing lens is not optimized for may experience an increase or decrease in flight time. It is possible to operate the TOF without the electrostatic lens, but this will reduce the acceptance cone from 3.8% to 0.1% of the full 4π steradians.

A table of maximum operating voltages for the various TOF system components is shown in Table 6.1.

Table 6.1: Operating Voltages of TOF Components

Electrode	**Max. Voltage**
Drift Tube	-200/+100
Lens	+1000
MCP	+2300
P7887 Start	$\pm$1.7
P7887 Stop	$\pm$1.7

Chapter 7

Stability and Delay Stepping

This chapter shows the processes for both stabilizing the experiment and for stepping through timing delays for FROG-CRAB. Stability ensures that the data collection is accurate. If the optical setup fluctuated under external vibrations, the timing between the attosecond and streaking pulses would vary. This would result in photoelectron measurements that were streaked by a field amplitude that was physically different than what the data was recording. The only change in timing delay between attosecond and streaking pulses should be initialized by a controlled scheme. This is the responsibility of the system designed to step through delays at known intervals and at coordinated times within the FROG-CRAB experiment's routine. As will be demonstrated, the mechanism for stability and controlled delay stepping are intimately related.

7.1 Stability

7.1.1 Types of Noise

Stability is necessary at the sub-wavelength scale. In the chapter on design goals, we noted that fluctuations of several hundred nanometers in the optical path difference between attosecond and streaking pulses would result in the photoelectrons experiencing a streaking effect from a IR field that has an amplitude very different from

what is assumed. Relative to the attosecond pulse, the 35fs, 800nm IR streaking pulse is effectively a continuous waveform. If the optical path difference were to shift by 400nm, the photoelectrons would see an IR field of reversed polarity. This is patterned on to the photoelectrons' energy spectrum. Because we assume a collection rate of fifty photoelectrons per second (one for each of the fifty shots per second), it is necessary to invest several hours to build a reliable histogram of flight times. Low-frequency drifts in the optical path, such as those due to thermal changes, would effect the entire experiment by imparting a false phase shift to the streaking field.

FROG-CRAB collects data at the 1kHz oscillator repetition rate. High-frequency noise (up to kHz level) from mechanical vibrations would effect the data by broadening the photoelectron spectrum. This is due to the random phase added to each photoelectron streaking event on a shot-to-shot basis, different from thermal drifts that affect the system over several hours. Whereas the thermal drifts will give a gradual "shift" to the time delay dependence of the dataset, high-frequency noise will pollute individual spectra at fixed delay times.

7.1.2 Stabilization with HeNe Interferometry

A typical Michelson interferometer is shown in Fig. 7-1. Using a 633nm Helium Neon laser (HeNe), the interferometer pattern can show variations in optical path difference between the two arms on the order of nanometers (small fraction of a wavelength). The power on the detector in Fig. 7-1 will vary with the path difference. Thus, if we observe the intensity on the power detector as a function of time, we can sample the frequency spectrum of the noise in the setup.

Interferometric stabilization to a fraction of the HeNe wavelength ($\lambda = 800$nm) will significantly reduce the potential statistical noise.

The choice of a HeNe laser is motivated by several factors. HeNe lasers are commercially available and economically viable. The technology is common in optics and the stability of commercial HeNe lasers is a well-understood property. Additionally, HeNe lasers may be several watts in continuous-wave power; however, for the purposes of interferometric stabilization a few milliwatts will suffice.

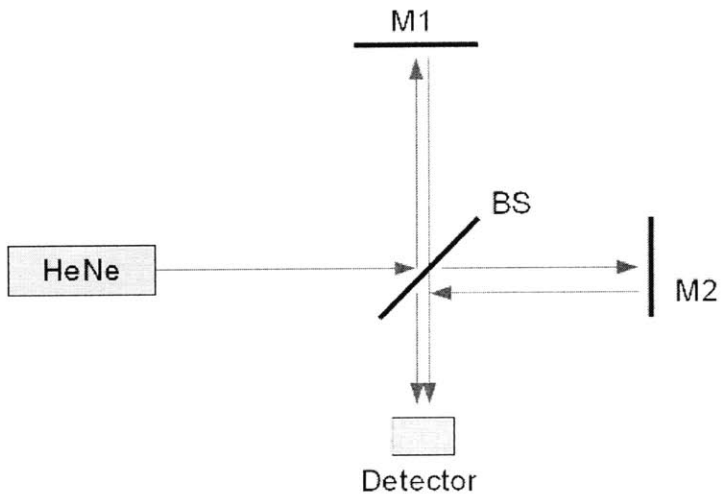

Figure 7-1: A typical Michelson interferometer. A monochromatic, 633nm HeNe laser is directed through a beam splitter (BS). The laser is split and both paths reflect from mirrors 1 and 2 (M1, M2). The laser recombines co-linearly and is sent to the detector. Given the net path difference between the two arms (up to modulus 2π), the intensity changes according to the interference of the two laser fields. To conserve energy, power is reflected back to the HeNe source (also dependent on the relative phase mismatch between the two paths).

Inserting the HeNe 633nm beam into the FROG-CRAB experiment is done by exploiting the bandwidth of the optics normally used for the 800nm IR femtosecond pulses. The exact positioning of the optics will be detailed in the following chapter. Commercially-available mirrors from CVI, model TLM, are used to beam steer the 800nm IR pulses. These mirrors are dielectric and so have a limited bandwidth of efficient reflection. The HeNe 633nm is partially reflected by the TLM mirrors; thus, the TLM dielectric mirrors act as beam splitters for the HeNe laser. By positioning the HeNe beam behind a TLM mirror, the transmission of the HeNe laser can be made to combine co-linearly with the IR driver pulse. Silver mirrors are used as well as the TLM model, and the reflection from silver mirrors is nearly 100% for HeNe as well as 800nm IR. The HeNe effectively propagates co-linearly with the IR pulses throughout the entire FROG-CRAB system. Because the HeNe has a continuous wave output, the intensity of the beam is very low compared to the peak intensity of each IR pulse. This makes the effect of the HeNe laser on HHG and FROG-CRAB negligible. By having the HeNe beam travel the length of the driver and streaking

paths, the two beams can be recombined in a Michelson interferometer setup.

The photodetector in the Michelson interferometer is a "balanced detector". A balanced detector has two photodiodes, which are used together to eliminate power fluctuations in the laser by looking at the *difference* between the two measured intensities. In a perfectly stable Michelson interferometer, a power fluctuation in the HeNe will increase or decrease the intensity measured on a single photodiode. This may be interpreted by the electronic feedback as a mechanical vibration. In a balanced detector, by subtracting the intensities from the two photodiodes we eliminate common noise, such as a power fluctuation in the HeNe.

In Fig. 7-1, we see only one beam terminating at a photodetector in the traditional Michelson interferometer setup. In Fig. 7-2 the photodetector actually has two inputs (photodiodes). Additionally, the setup in Fig. 7-2 has two beam splitters. This setup has two improvements over the traditional Michelson interferometer in Fig. 7-1. The first advantage is that the two beam splitters create two beams with an interference pattern. These two beams go to the two photodiodes on the balanced detector, which allows us to perform the balanced detection scheme by looking at the difference between the two measured intensities. The second improvement is the elimination of a "back reflection" into the HeNe. In the traditional Michelson setup, a perfectly aligned system would have some power going to the HeNe. This can cause thermal fluctuations from the power in the beam and interfere with the stable spatial modes. Balanced detection gives us the resolution in noise that is necessary for stabilization.

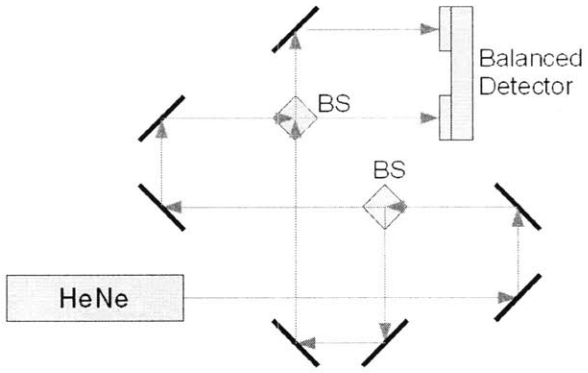

Figure 7-2: This balanced detector setup eliminates back reflection into the HeNe and common noise.

7.1.3 Stability Feedback

Using optics, we are able to send the recombined HeNe beam out of the vacuum chambers. This recombined beam is directed onto a photodetector, which measures the intensity. Any fluctuations in the path length difference between the driver and streaking pulses will be patterned onto the recombined HeNe beam because the HeNe travels along both paths. When the optical path difference between the two arms is constant, the power on the photodetector will also be constant. It may be that the path length difference is constant but nonzero. A constant offset is easily fixed with temporal alignment techniques. Alternatively, the phase offset can be taken as the first timing delay for the experiment. The goal of stabilization is to reduce external vibrations, not to correct for DC errors.

Stabilization works by "locking" the interferometric power on the photodetector to a set point. This means that the stabilization system will try to keep the power at the set point. The stabilization system interacts with the optical paths by using a piezoelectric translation stage with a mounted mirror. Because mirrors in a retroreflector configuration ideally have the laser beam at a 90 degree incidence angle, a piezoelectric-controlled retroreflector can change the net optical path length by mechanically translating along the beam trajectory. Fig. 7-3 shows how a piezoelectric stage can be configured to change the optical path length. For a translation of x, the optical path changes by $2x$ because the beam must return at the same angle.

Piezoelectric stages are capable of precision on the nanometer scale. In our FROG-CRAB setup, we use the Piezo Jena model PU40. This stage has nanometer precision and a maximum translation of 40μm. 40 microns is a large travel range, spanning tens of wavelengths at 633nm. A mechanical vibration or mirrors causes a phase error of no more than a few wavelengths, which is well within the 40 micron travel range. In the case of thermal drifts, where the expansion of metal actually changes the dimensions of the experimental setup, a slow displacement of many wavelengths is possible. The capability for the piezoelectric stage to translate many microns may be necessary. The PU40 was chosen because it is capable of both fast response and

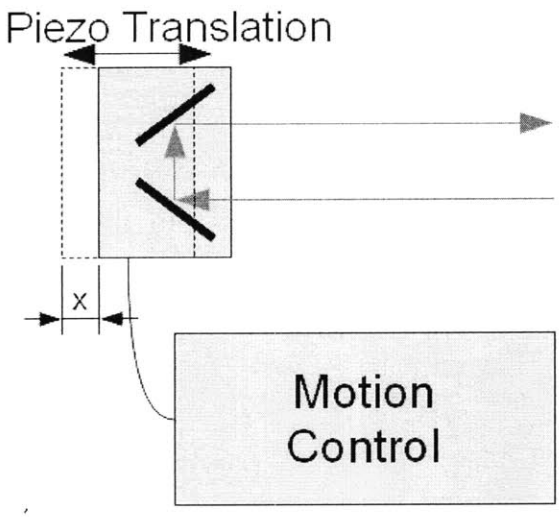

Figure 7-3: In the configuration shown here, the piezoelectric translation stage has a mounted retroreflector. External motion control moves the stage and optics assembly. For a movement of x, the optical path changes by $2x$ because the beam returns at the same angle.

large travel range.

The PU40 has a mechanical resonance at about 1kHz. If a control signal tries to drive the PU40 at 1kHz, it is possible to damage the model because of the resonant response of the unit. This fact constrains us to drive the PU40 at no more than few hundred hertz. Additionally, the 1kHz repetition rate of the driver pulse implies that we can identify noise at a maximum frequency of 500Hz (Nyquist sampling theorem). Empirically, interferometric measurements of the vibrational noise in the area surrounding the FROG-CRAB experiment revealed that the bandwidth of external noise is no more than 100Hz, so the PU40 can compensate for this error.

The PU40 operates by flexing a mechanical joint as a function of applied voltage. The acceptable voltage range is from -10 to 150V. This range corresponds to the full 40 microns motion. During the experiment, the resting position of the piezoelectric stage is at an applied voltage of 50V. Then, a higher or lower voltage can move the stage in or out, respectively.

The voltage is controlled by a feedback loop, which reads the intensity on the photodetector as input. This feedback loop has proportional and integral (PI) gain. The feedback system is the commercially-available Newport Corporation model LB1005.

The LB1005 has 10MHz of bandwidth, which is the frequency range in which it can correct for noise. It outputs in $\pm$10V, which is then amplified with a $\times$10 gain before being sent to the PU40. The LB1005 is used because of its good bandwidth and because it is easy to change some of the proportional and integration feedback parameters. In particular, the P-I corner, which is a property of the feedback gain, can be changed. Ideally, the P-I corner is set as low as possible given the noise bandwidth. For example, the noise in our FROG-CRAB is typically less than 100 Hz. Thus, a P-I corner of 100Hz functions well in our setup. Low-frequency thermal drifts (which fall within the P-I corner) are also compensated with the LB1005.

7.1.4 Experimental Startup

On startup, the HeNe is turned on and allowed to come to thermal equilibrium. The spatial modes of the HeNe change slightly as the metal casing undergoes thermal expansion. As the HeNe is coming to thermal equilibrium, the LB1005 is also turned on and its output connected to an oscilloscope. The LB1005 has a DC offset control knob. The DC offset must be set to 5V, as this will be amplified to be the 50V resting position of the PU40.

Once in thermal equilibrium, the HeNe is sufficiently stable for the experiment. Optics are checked for alignment and overlap after recombination. The exact optics setup will be detailed in the following chapter. Once the two arms are well-aligned at recombination, the photodetector is turned on and its output connected to the LB1005. An oscilloscope monitors the input to the LB1005 (measured intensity on photodetector output) as well as the LB1005's output, which is the feedback signal sent to the PU40 via a $\times$10 gain amplifier. The input to the LB1005 is a signal that is measured by a balanced detector. In order for the balanced detection to be meaningful, there should be no DC component. A DC component implies that one of the two photodiodes is receiving more average power. This could be due to absorption and attenuation in one path that is not balanced by the other. The standard procedure is to either use irises in front of the photodiodes to make the average power equal in both or to tune the LB1005 input to electronically remove the

DC component.

When balanced detection is obtained and a 5V offset set, the PU40 amplifier is turned on. We watch the control signal that is sent to the PU40 on the oscilloscope. This signal can show if the PU40 has struck its travel limit (0 or 40 microns). Such an event signifies that the LB1005 feedback is not properly set. Changing the P-I corner or the gain of the feedback will bring the feedback loop into a stable configuration. With the LB1005 properly set, the PU40 should move to compensate any external noise to the system, including low-frequency thermal drifts. This stabilization system should be able to remain locked for hours.

7.2 Delay Stepping

The PU40 piezoelectric stage is responsible not only for stabilization but also for changing the timing delay between the attosecond and streaking pulses. If the PU40 can be controlled to move a known distance, this would correspond exactly to a known time delay. The challenge is to control the PU40 with accuracy and precision. Experimentally, the PU40 is controlled directly by the LB1005 feedback loop. It is inadvisable to attach another signal to the PU40. A better practice is to influence the output of the LB1005 by changing the balanced detector signal. Common noise is eliminated in a balanced detection setup; thus, only by changing the interference result on the balanced detector may we affect the feedback loop.

7.2.1 Phase Advancer

The method for changing the interference pattern is to impart a known phase advance to the HeNe beam in one of the arms. The phase advance would change the interference pattern accordingly, which the LB1005 will compensate by moving the PU40. For example, a phase advance of pi will cause the LB1005 to move the PU40 stage by a quarter wavelength at 633nm (quarter because of the $2x$ relationship between stage displacement and optical path change). Remembering that the HeNe beam takes the same path as the IR streaking pulse, any change in the optical path caused by a

known phase advance will also change the optical path of the streaking pulse, which in turn represents a known timing delay step.

The phase advancer we use is a modification of an Evans phase shifter [16] and a Pancharatnam screw [17]. In the beam path of one of the arms we place three waveplates, shown in Fig. 7-4.

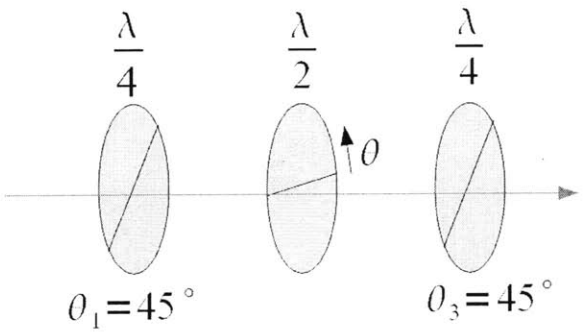

Figure 7-4: This assembly of three waveplates ($\frac{\lambda}{4} \rightarrow \frac{\lambda}{2} \rightarrow \frac{\lambda}{4}$) changes the phase of the HeNe beam in a controllable way. The angle of the half-waveplate determines the exact phase advance.

The effect of the phase advancer assembly can be represented by a matrix. In the Jones vector formation, the result of propagating through the phase advancer assembly is given by:

$$\begin{pmatrix} e^{-2j\theta} & 0 \\ 0 & -e^{2j\theta} \end{pmatrix}. \tag{7.1}$$

Assuming the HeNe is polarized correctly, Eq. 7.1 shows that the result of propagating through the phase advancer assembly is a phase change of $2j\theta$. If we want to advance a full wavelength, θ should be rotated to 180 degrees. The form of Eq. 7.1 also shows that if we rotate the middle waveplate continuously, the phase imparted to the HeNe beam will advance continuously as well.

When we adjust the phase advancer, the effect is similar to that of thermal expansion. The LB1005 will see a low-frequency change in the balanced detector output. It will respond by sending a compensating signal to move the PU40 an amount related to how much the half-waveplate is rotated. A vacuum-compatible rotation stage holds and rotates the waveplate. This rotation stage is controlled by electronic hardware

that can interface with Matlab. As with the data acquisition, Matlab coordinates the rotation of the waveplate, which in turn dictates the phase advance and timing delay steps. The timing delay step size and the total number of delays can be chosen by the user.

Chapter 8

Experimental Layout

This chapter records the vacuum chamber and optical path layout for the FROG-CRAB experiment. The design was partially constrained by the existing HHG vacuum chamber and available work area, but the FROG-CRAB additions were motivated by the goals discussed in previous chapters.

8.1 Overall Layout

An overhead schematic of the FROG-CRAB experiment and surrounding area is shown in Fig. A-2 in the Appendix. The light blue area is the optics tables. This defines the available surface for the experiment. Some of the design decisions were taken on the basis of confined workspace. Part of the setup involves steering the IR pulses from the amplifiers to the FROG-CRAB experiment. To do this, we use CVI two inch dielectric (TLM) mirrors. An expanding telescope enlarges the beam waist, which reduces the self phase modulation (SPM) that would otherwise distort the pulse shape. SPM depends on the intensity of the pulses, so by spatially expanding the beam waist the peak intensity is reduced. A contracting telescope reduces the beam waist to the desirable size near the first of the vacuum chambers.

In total, the FROG-CRAB assembly contains three principle vacuum chambers. Each connection between these vacuum chambers is equipped with a manually-operated valve that can be used to isolate individual chambers. The first vacuum chamber,

"HHG chamber", is the original chamber installed during the HHG experiments. The second chamber, "TM chamber", holds the toroidal mirror for focusing the attosecond pulses and also holds the phase advancer. The final vacuum chamber is the "TOF chamber". This chamber contains the gas jet and TOF nozzle where the FROG-CRAB streaking interaction takes place.

Each vacuum chamber is pumped by a turbo (various models and speeds) with an attached roughing (scroll) pump. These pumps keep the vacuum chambers at safe operating pressures. The operating pressure is different for each chamber and detailed in Fig. A-3 in the Appendix. Connected at the end of the TOF chamber is the spectrometer used for XUV measurements. By interchanging the grating, different frequency ranges can be measured if desired.

An explanation of the three vacuum chambers will show the different uses for each.

8.2 HHG Chamber

Because FROG-CRAB is fundamentally an optics experiment, the optical layout dictates in part the vacuum chamber system. Fig. A-4 in the Appendix shows the general optics layout and corresponding vacuum chambers. The original purpose of the HHG chamber was to host the HHG system; now, its versatility has been exploited to include the beam splitter for the HeNe beam and IR pulses as well as the rough temporal alignment and piezoelectric stages.

The gas cell is located inside the HHG chamber. The IR driver pulses are focused into this gas cell by a silver mirror that is positioned 50cm inside a tube attached to the HHG chamber. The purposes for this tube attachment are twofold. First, as seen in the layout in Fig. A-4, the angle of incidence into and out of the tube is close to normal. For a circular mirror, astigmatism is reduced the closer the incidence angle is to normal. By keeping the astigmatism low, the tube attachment serves to protect the spatial profile of the IR driver pulses.

A second reason for the tube attachment is to allow the circular mirror to have a long focus length. Gouy phase shift is higher for shorter focal lengths, a fact that

can cause phase matching problems for HHG. One potential solution to reduce Gouy phase without a tube attachment would be to place a focusing element inside the HHG chamber before a final flat mirror that steers the IR into the gas cell. This is not done because once the IR is focused, its beam waist begins to shrink and the peak intensity rises. If the focusing IR beam strikes any optics during its focusing, the beam is likely to damage the optic. This damaging occurs because of the increased peak intensity when the IR is focused. By making the final optic a long-focal length mirror that also steers the IR pulses into the gas cell, we eliminate the risk of damaged optics.

The beam splitter can be either a neutral density filter (ND filter) or a beam sampler designed for 800nm IR pulses. Either optic can be changed to split at desired percentages. The majority of power should go into the HHG gas cell for attosecond generation. A smaller fraction can be taken for the streaking pulse.

After the beam splitter, the streaking pulse (and co-linear HeNe beam) passes through a rough temporal alignment retroreflector. This retroreflector is mounted on a vacuum-compatible, motorized translation stage. The stage can be controlled either by a computer using Matlab or by using the hardware interface directly. Moving the retroreflector will change the optical path and hence the temporal delay between the attosecond and streaking pulses. In addition to the rough temporal alignment stage, a piezoelectric stage is also placed in the HHG chamber for stabilization and timing delay stepping. This is accomplished by the PU40 stage described in a previous chapter. The PU40 stage is located in the streaking pulse optical path after the rough temporal alignment.

The HHG chamber has two exit ports, one for the attosecond pulses and one for the streaking pulses. The HeNe beam travels through both of these exit ports. Most of the IR driver pulse remains after the HHG gas cell and is co-linear with the produced XUV.

8.3 Toroidal Mirror Chamber

The second chamber of the FROG-CRAB apparatus is known as the toroidal mirror (TM) chamber. A schematic of this chamber is shown in Fig. A-5 in the Appendix. The TM chamber houses four major components: the toroidal mirror, the aluminum filter, the phase advancer, and the recombination optics. The decision to place these components in a separate chamber (TM chamber) as opposed to inside the HHG chamber was based on several reasons. A primary concern was space allocation inside the HHG chamber. When the HHG chamber was designed, it was not anticipated that many additional components would be used. A new chamber was necessary to house the FROG-CRAB elements.

An important reason for designing a new chamber is to hold the aluminum filter. In the previous configuration, the aluminum filter was part of the HHG chamber. The high intensity IR driver pulse, which retained most of its pulse energy after HHG, could damage the thin aluminum filter. Because the beam expands due to diffraction, increasing the distance between the focal point (the HHG gas cell) and the aluminum filter would reduce the peak IR intensity on the filter's surface. Designing a new vacuum chamber to hold the aluminum filter solved this problem.

A final reason for using the TM chamber is to isolate the different optics components. Whenever the experiment is aligned, elements changed, or new components are installed, it is necessary to access different parts of the setup. By isolating the different components in separate chambers, we reduce the problems associated with breaking vacuum and servicing the interior of the vacuum chambers.

The toroidal mirror inside the TM chamber has a focal length of about 40cm. The particular alignment as seen in Fig. A-4 was designed to accommodate the surface area available in the laboratory. When the aluminum filter was moved to its present location, the toroidal mirror focal length was set by the minimum operable distance from the gas cell and after the aluminum filter. The toroidal mirror was prepared by McPherson as a custom order. The incident angle of four degrees is taken because the gold-coated surface reflects XUV well at that incidence angle. This four degree

incidence angle accounts for the placement of the exit port, which is designed to be at the position that a beam would strike the chamber wall after an eight degree reflection deviation from horizontal.

The TM chamber is also where the combination of the attosecond and streaking pulses occurs. A drilled mirror, shown in the layout in Fig. A-4, is used to make the streaking and attosecond pulses co-linear. No dichroic mirrors exist in the XUV wavelength; instead, the center of a regular silver mirror is drilled to allow the XUV to pass. A spatially-broad streaking beam is focused onto the outer rim of the drilled silver mirror such that most of the beam is reflected into a co-linear propagation with the attosecond pulses. Although the center of the streaking pulse is lost due to the drilled section of the mirror, enough optical power is reflected to be used in FROG-CRAB.

A separate window on the left side of the TM chamber serves as an exit for the IR pulses during rough alignment. During rough temporal alignment, the aluminum filter is removed and no gas is let into the HHG gas cell. HHG does not happen and the IR driver pulse is not screened by the filter. Instead, a separate translation stage moves a "pick-off" mirror into the beam trajectory. This mirror is shown in Fig. A-4. The IR pulse, which was split by the beam splitter in the HHG chamber, is still recombined by the drilled mirror. The recombined pulses are reflected by the pick-off mirror out of the TM chamber via the window. Once outside, overlap detection is used to ensure that the optical path difference between the driver and streaking pulses is roughly zero. The piezoelectric stage is used for fine-tuning the path difference.

Finally, the phase advancer is also located in this chamber. A second window at the top right of the diagram in Fig. A-5 is used as an exit port for the HeNe beam. A drilled mirror is placed in front of the aluminum filter (as seen in Fig. A-4) that passes the attosecond pulses but captures part of the broad HeNe beam. The HeNe is sent through the phase advancer and recombines with the portion that traversed the streaking pulse path. This recombined HeNe beam is sent out of the TM chamber into a balanced detection scheme.

8.4 TOF Chamber

The final vacuum chamber is the TOF chamber. This chamber holds the gas inlet for FROG-CRAB and the TOF nozzle. The TOF chamber is shown in Fig. A-6 in the Appendix. An external control pad is able to move the gas inlet nozzle in three dimensions. This is used to position the gas inlet such that the escaping gas directly impinges on the co-linear XUV and IR streaking pulses. Together, the gas inlet direction and beam propagation direction form two axes. The third axis is made from the TOF nozzle, which is the front end of the drift tube. The center of these three axes is the interaction region, where the XUV ionizes atoms to emit photoelectrons, which are subsequently streaked by the IR pulse. The decision to place this interaction region into a separate vacuum chamber was based on the desirability for keeping the TOF instrument under vacuum. It is rarely necessary to expose the gas inlet and TOF to atmosphere, whereas the other components in the FROG-CRAB experiment may need to be serviced or aligned more regularly. By including the TOF chamber in the FROG-CRAB experiment, we have managed to reduce the potential risks involved in exposing the TOF instrument to atmosphere.

Chapter 9

Organizing an Experiment

To aid in understanding the FROG-CRAB experiment, it is useful to step through the process of an example measurement. In the recently submitted paper by Huang et al [18], the framework for generating a single, 200as, uncompressed attosecond pulse was presented. In the chapter on HHG theory, we learned that a train of attosecond pulses is produced by a driver pulse with multiple cycles. Although a train of attosecond pulses is a useful accomplishment, a single attosecond pulse is more versatile for pump-probe experiments [19]. In this chapter, we review some calibrating steps for a FROG-CRAB experiment to measure the hypothetical, single-cycle pulse in [18].

Producing a single attosecond pulse has traditionally been sought by using various "gating" techniques, which are schemes to limit the optical power imparted to all but one attosecond pulse in a train [20, 21, 22, 23]. The technique employed by Huang et al is to use a single-cycle IR driver, shown in Fig. 9-1. The single cycle of the IR driver pulse, centered at about 1.5 microns, ensures that XUV is only generated once in the interaction region. HHG will result in an isolated XUV pulse with a spectrum that spans approximately 50-300eV and spanning a few femtoseconds, shown in Fig. 9-2. The efficiency of the HHG using this single-cycle IR driver is low, around 10^{-8}.

Numerically, it is predicted that the lower end of the XUV spectrum will have a highly nonlinear chirp. Eliminating this highly nonlinear section of the spectrum will result in a 200as pulse. Although we lose bandwidth when we remove this part of the spectrum, the highly nonlinear chirp caused the pulse to be much broader in time.

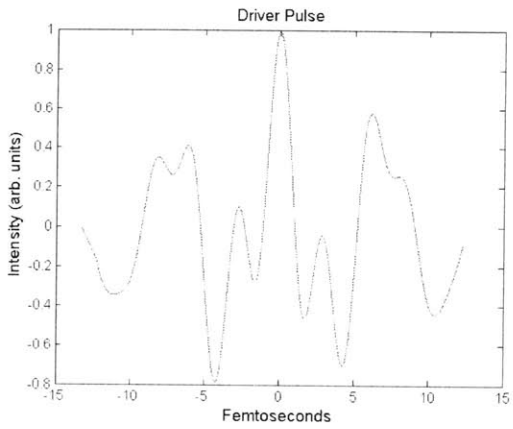

Figure 9-1: The single-cycle IR driver pulse is used to generate an isolated XUV pulse.

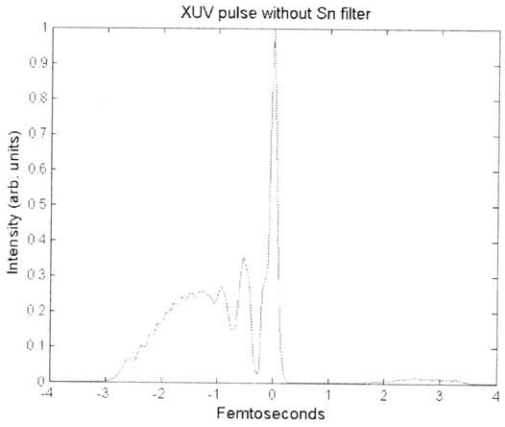

Figure 9-2: The temporal intensity profile of the XUV pulse generated by the single-cycle IR driver. The lower, nonlinearly-chirped portion of the spectrum is retained in this plot. No tin filter has been applied.

Filtering is done with a tin sheet, which is a high-pass filter above 70eV. The filtered XUV pulse is shown in Fig. 9-3.

The XUV pulses can be measured using Argon gas in a FROG-CRAB experiment. We need to understand how to design this FROG-CRAB measurement; namely, we should determine the approximate gas flow rate to be used at the TOF interaction region and the acquisition delay for the TOF/MCA.

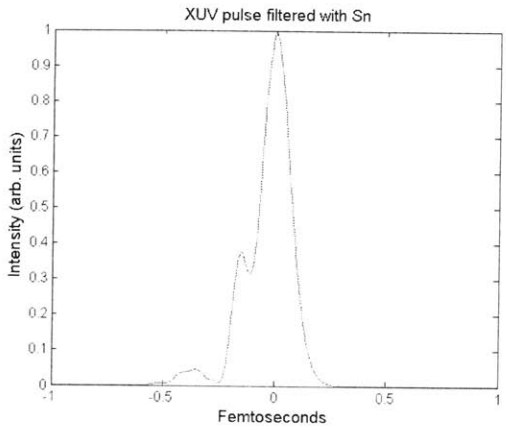

Figure 9-3: The temporal intensity profile of the XUV pulse after being filtered by a tin sheet.

9.1 Gas Flow Rate

As detailed in previous chapters, vacuum pressure is an important operating consideration. It is necessary to maintain appropriate vacuums for the equipment to function properly. This is particularly true in the TOF chamber due to the sensitive MCP at the back of the TOF instrument. Although the motivation to keep the gas flow rate low in this chamber, there may be an advantage to increasing the flow rate so the FROG-CRAB interaction is not gas-limited. A gas-limited FROG-CRAB experiment is one in which the number of gas atoms is low relative to the number of XUV photons. This imbalance results in a photonelectron collection rate that is undesirably low. Conversely, a photon-limited experiment is one in which there are more gas atoms than can possibly interact. The photoelectron collection rate is still low in this scenario, but there is an additional danger to the system because the unnecessarily high gas flow may cause the pressure to rise above a safe level. Experimentally, it is much easier to change the gas flow rate using the Sierra Smart Trak 2 regulator. By matching the gas flow rate with the available XUV photon flux, we can achieve the best photoelectron collection rate per gas flow.

In this particular setup, we expect to have 1mJ driver pulse energy with an HHG conversion efficiency of 10^{-8}, which implies that the XUV pulses will be 10pJ. In order to estimate a gas flow rate, we need to know the number of XUV photons available

per shot. Although the XUV photons cover a spectrum, a good approximation is to take the center frequency to find the number of photons in the XUV pulse. Now, we take the center energy to be 150eV, which leads us to find that

$$N_\gamma = \frac{10\text{pJ}}{150\text{eV}} \approx 400000. \tag{9.1}$$

We would like a gas flow rate such that the net result of the N_γ photons interacting with the gas produces one photoelectron count on the TOF MCP. The reason for choosing only one count per experimental shot is because the MCA is unable to measure two photoelectrons at the same time bin. If a measurement contains a large number of double-counts, which register only as a single photoelectron, the photoelectron energy spectrum will appear broadened. A one nanosecond difference in photoelectron flight time is related to about one eV of energy difference, so we expect the photoelectron flight time spread to be no more than forty or fifty nanoseconds. This corresponds to nearly 200 time bins. The probability of a double-count may seem low; however, the flight times obey a weighted distribution (this is what makes the photoelectron energy spectrum possible to measure with a TOF). This fact makes the chance of a double-count statistically significant. Thus, it is useful to try to tune the experiment to measure only one photoelectron per shot.

Heuristically, we know that the photoelectron collection rate is a function of four variables: the numbers of gas atoms and XUV photons in the interaction region, the ionization probability per XUV photon, and the TOF collection cross section. This is mathematically expressed as the following:

$$\text{Collection Rate} = N_\gamma N_{\text{atoms}} \times (\text{Ionization Probability}) \times (\text{TOF Collection Fraction}) \tag{9.2}$$

where N_γ is the number of photons for XUV pulse and N_{atoms} is the number of gas atoms available in the interaction volume. In practice, the best way to influence Eq. 9.2 experimentally is to change N_{atoms} via the Smart Trak 2 gas flow regulator. By changing the gas flow rate, we can increase or decrease the number of gas atoms avail-

able to interact with the XUV photons. The number of XUV photons is typically held fixed because of the optical components of the experiment. The ionization probability is also a fixed parameter, dependent on the gas used (in this case we choose Argon). Finally, the TOF collection cross section is determined by the aperture size of the TOF nozzle relative to the distribution of emitted photoelectrons. Photoelectrons are assumed to be emitted isotropically, so the rate of photoelectron collection is augmented by the geometric dimensions of the TOF nozzle's solid angle relative to 4π steradians. From the center of the interaction region, the TOF aperture forms a symmetric, 45 degree, full angle cone. This corresponds to a solid angle that is about 3.8% of the full 4π.

Although Eq. 9.2 is useful for understanding the theoretical basis for the photoelectron collection rate, in practice to find the optimum gas flow we use experimental means. The multichannel analyzer P7887's software interface window allows an experimenter to collect information about the collection rate and total counts. Additionally, it allows a user to set appropriate parameters such as acquisition delay, sweeps, number of time bins, and trigger thresholds. Among the options available is a setting for the sweep's region of interest (ROI), which is a portion of the time bins in each sweep that the user would like information about. This information includes statistics such as total counts and counts/second and it is available on the software interface window. When the parameters are set correctly, the ROI can focus on the photoelectron spectrum.

The optimum gas flow is found by setting the MCA for a preset number of sweeps and successively comparing the total number of counts in the photoelectron spectrum ROI as a function of changing gas flow rate. All other parameters of the system, such as the MCP voltage and the XUV pulse energy, are kept constant, because it is assumed that the XUV pulse energy is already maximized. Theoretically, we expect that the total number of counts in the ROI will increase with increasing gas flow rate until an asymptotic value is reached. The total number of counts asymptotes with increasing gas flow because of two reasons: we approach the photon-limited collection barrier and double-count events start to occur. Both scenarios are undesirable. An

example of this gas calibration technique is shown in Fig. 9-4. The gas used was Argon and the pulse energy was about 27pJ. The trend of increasing ROI counts with increasing gas flow is seen. In many experimental cases, we hit an upper limit of the safe operating vacuum pressure before the ROI counts begin to clearly asymptote.

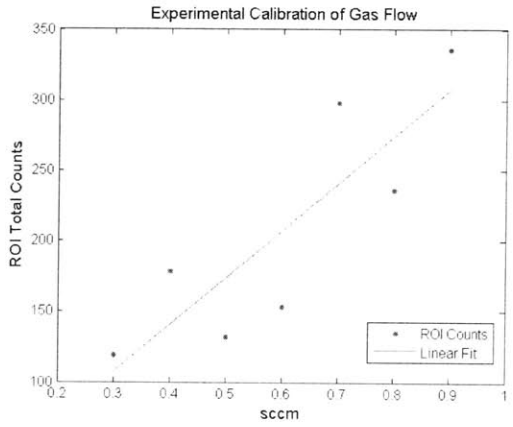

Figure 9-4: The total counts in the photoelectron spectrum recorded by the MCA after 20000 sweeps. The total counts increase with increasing gas flow. The linear fit is an approximate functional dependence that holds in the low-flow regime. In this measurement, the gas load into the vacuum chamber was prohibitively large at 1 sccm, although the asymptotic behavior of the ROI counts is not fully reached.

In addition to controlling the gas flow rate, we can also change the position of the gas inlet nozzle as well as the gas nozzle aperture size. These capabilities give us the option of influencing the ROI count rate without increasing the gas load into the vacuum chamber. Changing the position of the gas inlet nozzle allows us to find the optimum position for the escaping gas to interact with the XUV pulses. This can move the interaction region closer to or farther from the TOF opening. Likewise, the gas nozzle aperture size also influences the collection rate. The local density of the escaping gas depends on the aperture size. A larger aperture allows for a lower density at the same flow rate, while the converse is true for a smaller aperture.

Typically, a FROG-CRAB experiment will be limited by the vacuum pressure requirements. In the experiment to measure the 200as isolated XUV pulse, the situation is similar. We need to balance an increased collection rate with the increased danger to the MCP due to pressure-related concerns. Ultimately, the optimum gas flow rate

is found empirically by studying when the collection rate begins to asymptote with increasing flow rate.

9.2 Sweep Parameters

Following the discussion in the chapter on the TOF, we want to optimize the MCA's sweep parameters. The acquisition delay is an important parameter because it determines the beginning of the MCA event counter. To keep the dataset compact and efficient, we want to set the acquisition delay as long as possible without interrupting the measurement. We can use the result Eq. 6.1 from the chapter on the TOF and MCA in conjunction with the known XUV photon energies to estimate an acquisition delay. The XUV photons in [18] span 50-300eV. Argon gas has an ionization potential of about 15eV, so the photoelectron kinetic energies can span from 35eV up to 285eV (assuming no other losses). Given the TOF parameters and this energy range, we can numerically estimate the times of flight. The numerical results are shown in Fig. 9-5. The fastest photoelectrons dictate the longest acquisition delay. If we use an

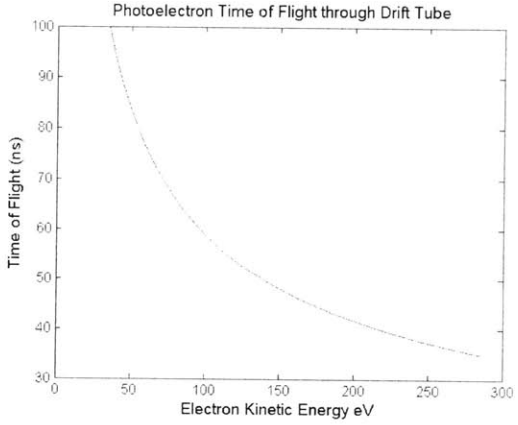

Figure 9-5: The numerically-computed flight times of photoelectrons with a broad range of kinetic energies (35-285eV). The acquisition delay should be set by the fastest photoelectrons.

acquisition delay that is longer than the fastest possible photoelectrons, part of the photoelectron spectrum is cut. From Fig. 9-5 we see that we want an acquisition delay of about 35ns, which corresponds to 140 time bins.

We also want to set the total number of time bins. Minimizing the total number of time bins helps with data storage by keeping the vector lengths short. Furthermore, the fewer time bins used reduces the total noise because it minimizes the number of recorded false events. One of the advantages of the MCA is that we can stop recording during dead times in between photoelectrons. The sweep length (total number of time bins) controls the active search period. Looking at Fig. 9-5, we see that the slowest photoelectrons take about 100ns to reach the MCP. Thus, we should not expect photoelectrons to arrive much later than a certain limit. In this case, we can set the total time bins based on the longest time, or 100ns $\sim$ 400 time bins. If we allow for streaking of 20eV by the IR pulse, we should increase the total time bins by 50ns = 200 bins to 600 time bins total. This reflects the effect of slowing the 35eV photoelectrons by 20eV to 15eV (flight time $\sim$ 150ns).

Calibrating the TOF is a process that depends on the experiment's parameters. The type of gas dictates the ionization potential, which is offset from the photoelectrons' final kinetic energies. These energies also depend on the properties of the XUV. In this experiment, we expect base photoelectron kinetic energies to span from about 35-285eV. After factoring in the signal delays due to cable lengths, the best procedure for calibrating the TOF is to compare the photoelectron spectrum to the XUV spectrum as seen by the spectrometer. This calibration is performed prior to initializing the complete FROG-CRAB measurement.

9.3 Additional Remarks

The systems of stabilization and delay timing step control were discussed in a previous chapter. While the stabilization feedback is passive, the delay stepping is actively controlled by the Matlab interface. The delay step size should be a fraction of the streaking pulse's central wavelength. If a streaking pulse does not have many cycles, as in the experiment discussed here, the delay step size should be temporally short enough to resolve the changes in the driver pulse's electric field. This can be accomplished by looking at the spectrum of the driver pulse and considering the sampling

criteria necessary for resolving the different frequency components. For the driver pulse in Fig. 9-1, we see that a delay step size of about 0.5fs $\rightarrow$ 150nm provides resolution sufficient to characterize the streaking pulse. At the HeNe wavelength of 633nm, this is about one quarter of the wavelength. To make a $\frac{\lambda}{4}$ step, the phase advancer half-waveplate should be turned 45 degrees.

Ultimately, the experimental parameters are to be set by the experimenter depending on the particular properties to be studied. A successful user of the FROG-CRAB system should understand its various components and be familiar with the algorithms used to retrieve temporal pulse profiles.

Chapter 10

Conclusion

In this thesis, I have explained the theory of HHG, reviewed the numerical algorithms of phase retrieval, and discussed in detail the various aspects of the FROG-CRAB apparatus. The FROG-CRAB experiment is a system rather than an isolated apparatus, and knowledge about the numerous components is required to successfully demonstrate phase retrieval. Looking to the future, I expect to measure ever-shorter attosecond pulses generated by state-of-the-art laser technology. Additionally, a plethora of scientific experiments are possible using FROG-CRAB. We will be able to measure different properties of atomic systems and observe the dynamics on an unprecedented timescale.

Appendix A

Figures

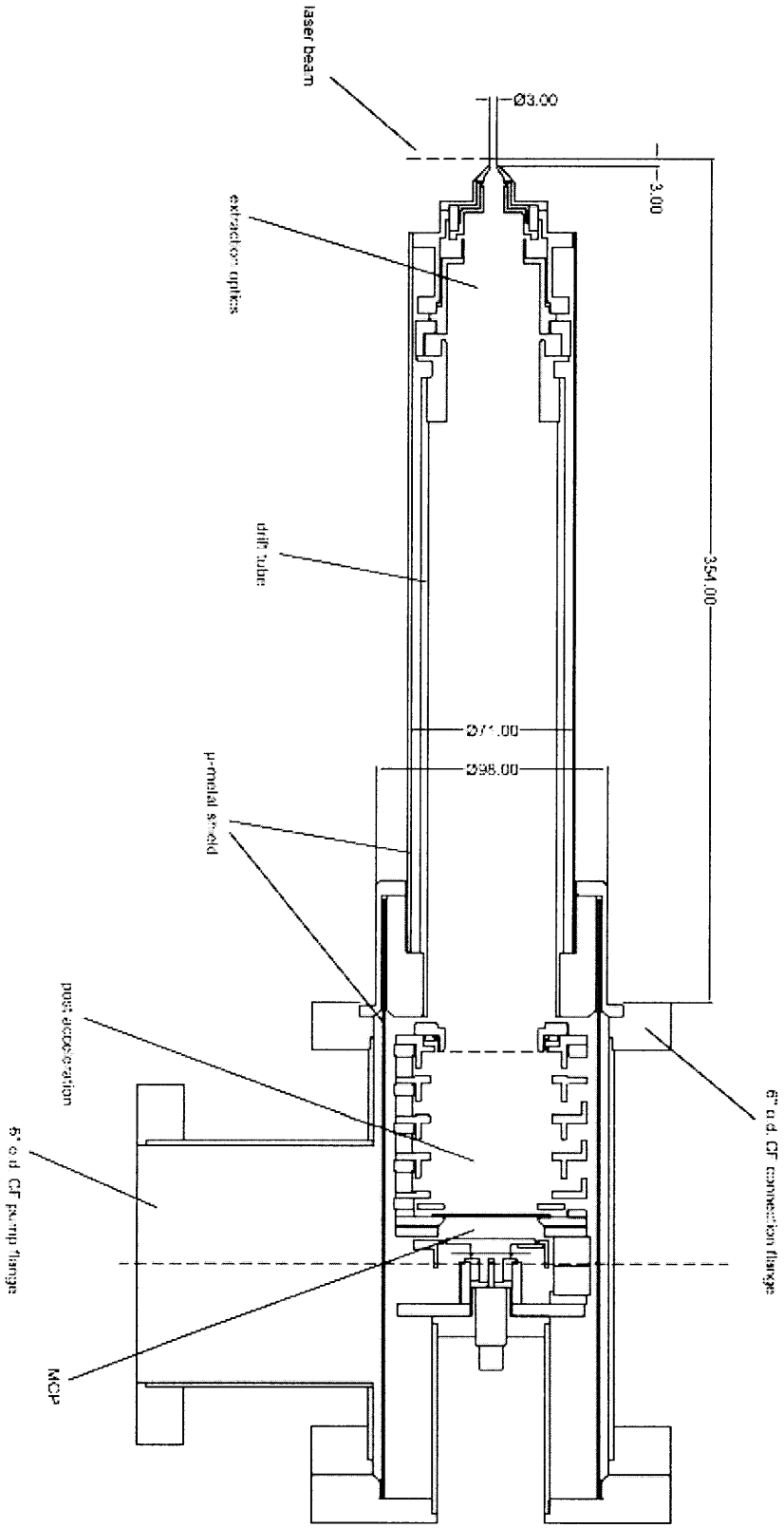

Figure A-1: This blueprint shows the design of the TOF instrument.

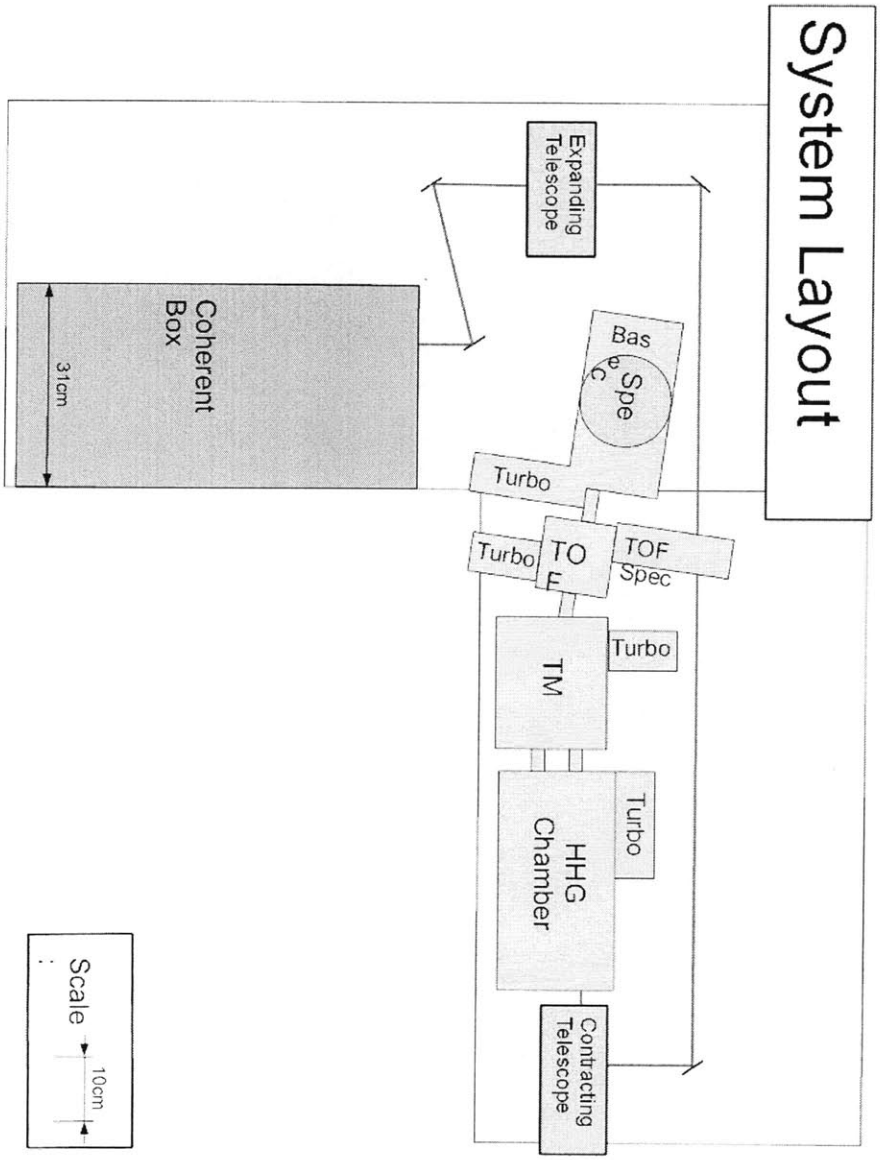

Figure A-2: An overhead view of the experimental layout, including the regenerative amplifier, beam steering, and FROG-CRAB vacuum chambers.

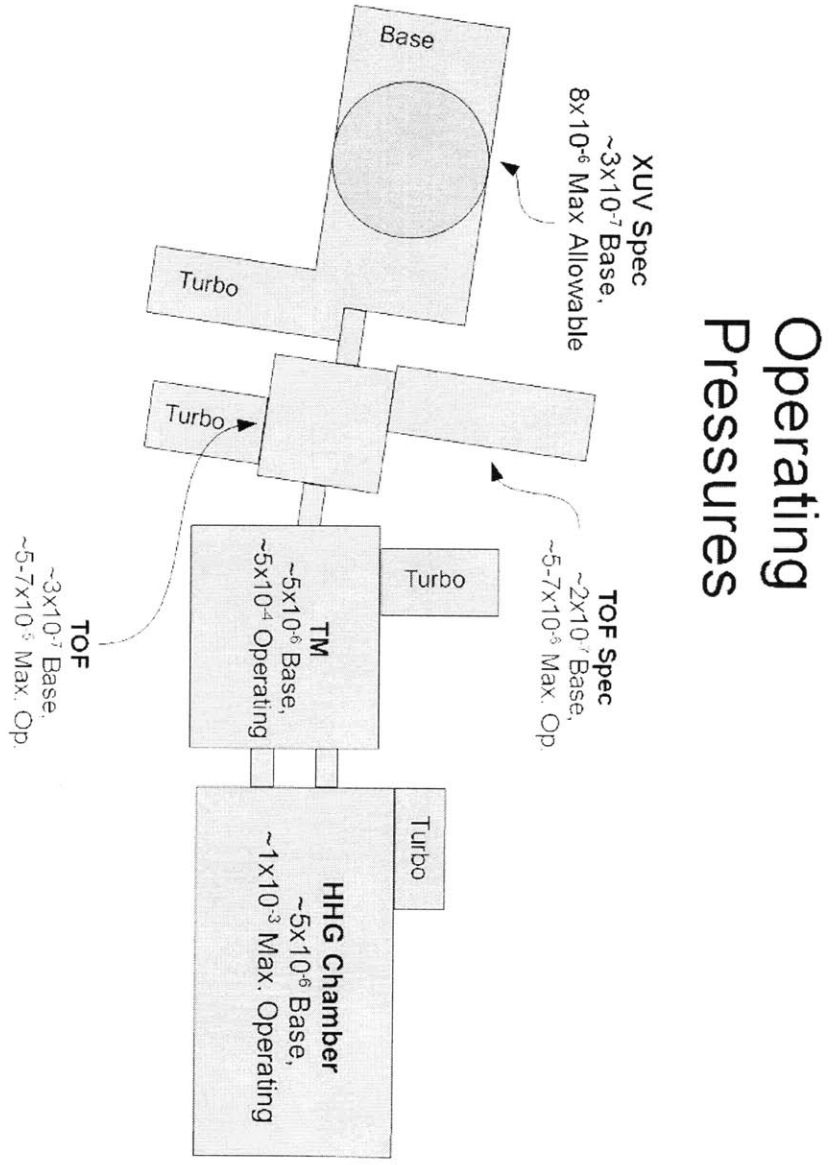

Figure A-3: This schematic shows the operating vacuum pressures of the FROG-CRAB experiment.

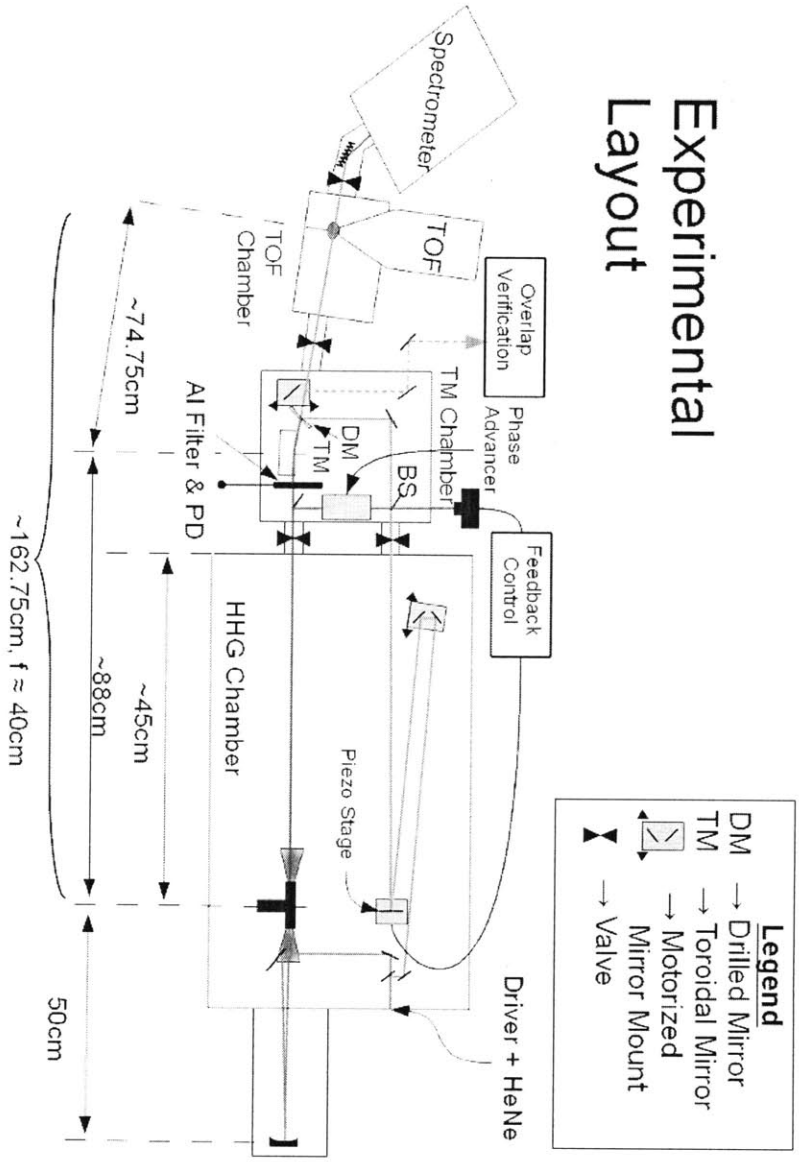

Figure A-4: A schematic of the experimental layout with the optical paths and dimensions shown. Thank you to Donnie Keathley for donating this schematic.

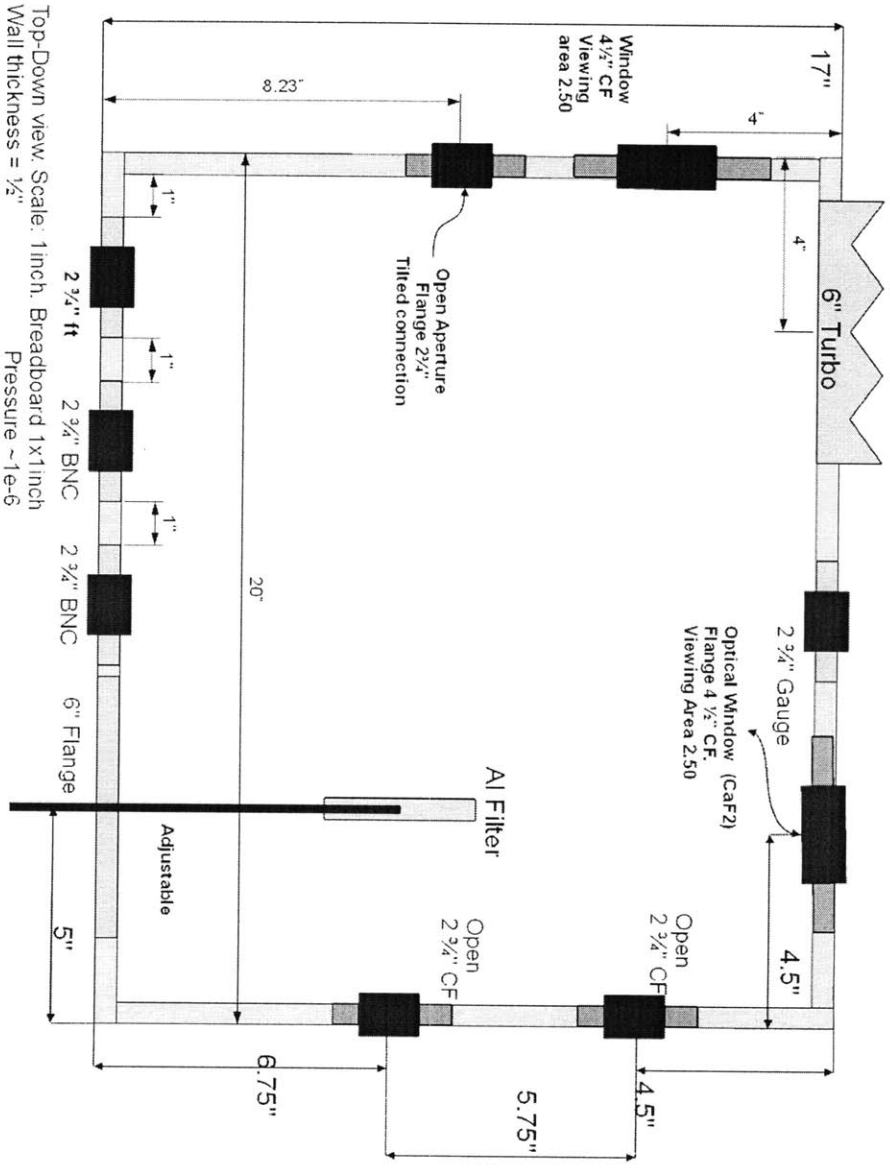

Figure A-5: This shows a schematic of the TM chamber, including its various ports and feedthroughs.

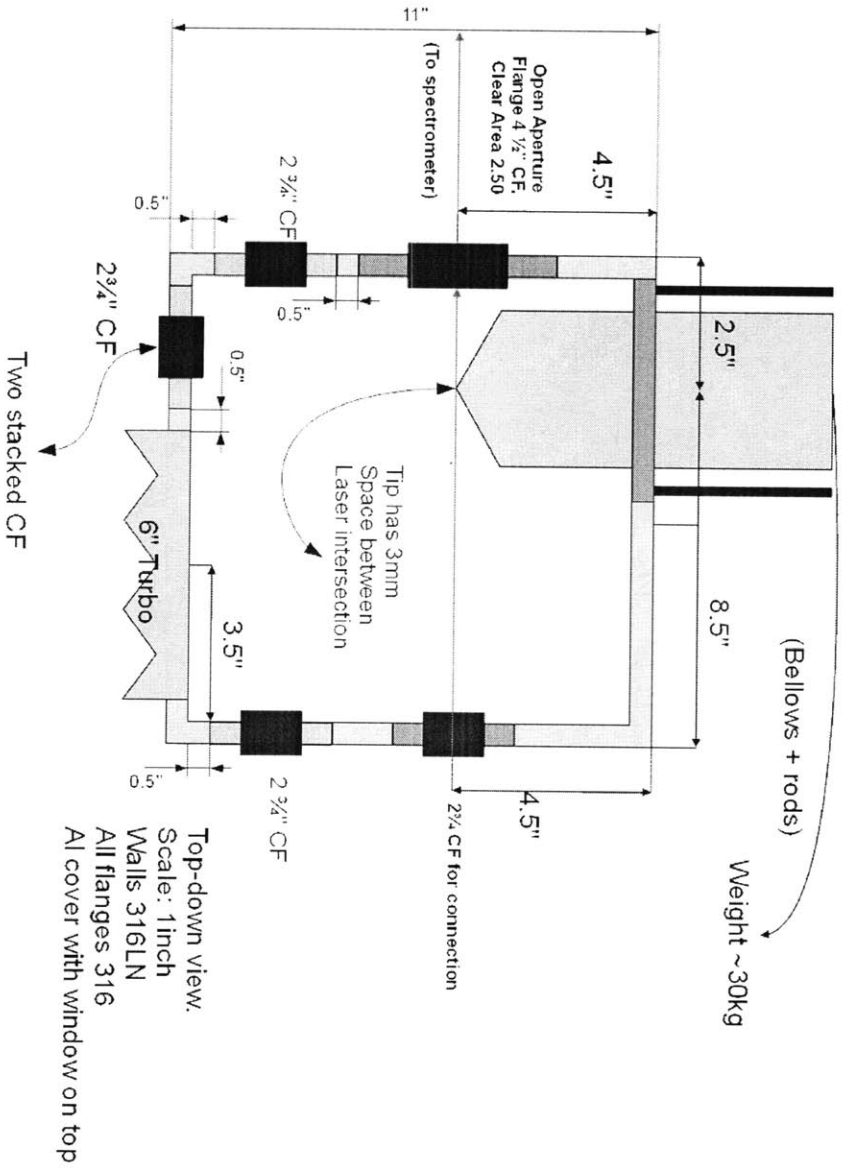

Figure A-6: The TOF vacuum chamber, which holds the gas inlet for FROG-CRAB and the TOF nozzle.

Bibliography

[1] Ferenc Krausz and Misha Ivanov. Attosecond physics. *Rev. Mod. Phys.*, 81(1):163–234, Feb 2009.

[2] M. Lewenstein, Ph. Balcou, M. Yu. Ivanov, Anne L'Huillier, and P. B. Corkum. Theory of high-harmonic generation by low-frequency laser fields. *Phys. Rev. A*, 49(3):2117–2132, Mar 1994.

[3] M Nisoli and G Sansone. New frontiers in attosecond science. *Progress In Quantum Electronics*, 33(1):17–59, January 2009. 000263211200002.

[4] P. B. Corkum and Ferenc Krausz. Attosecond science. *Nat Phys*, 3(6):381–387, June 2007.

[5] Thomas Brabec and Ferenc Krausz. Intense few-cycle laser fields: Frontiers of nonlinear optics. *Rev. Mod. Phys.*, 72(2):545–591, Apr 2000.

[6] P. B. Corkum. Plasma perspective on strong field multiphoton ionization. *Phys. Rev. Lett.*, 71(13):1994–1997, Sep 1993.

[7] M. Lewenstein, Ph. Balcou, M. Yu. Ivanov, Anne L'Huillier, and P. B. Corkum. Theory of high-harmonic generation by low-frequency laser fields. *Phys. Rev. A*, 49(3):2117–2132, Mar 1994.

[8] F. Qur, Y. Mairesse, and J. Itatani. Temporal characterization of attosecond XUV fields. *Journal of Modern Optics*, 52(2):339–360, 2005.

[9] D.J. Kane. Recent progress toward real-time measurement of ultrashort laser pulses. *Quantum Electronics, IEEE Journal of*, 35(4):421 –431, April 1999.

[10] Rick Trebino. *Frequency-Resolved Optical Gating: The Measurement of Ultrashort Laser Pulses*, chapter 5, pages 106–108. Kluwer Academic Publishers, first edition, 2000.

[11] Y. Mairesse and F. Quéré. Frequency-resolved optical gating for complete reconstruction of attosecond bursts. *Phys. Rev. A*, 71(1):011401, Jan 2005.

[12] O. Hemmers, S. B. Whitfield, P. Glans, H. Wang, D. W. Lindle, R. Wehlitz, and I. A. Sellin. High-resolution electron time-of-flight apparatus for the soft x-ray region. *Review of Scientific Instruments*, 69(11):3809, 1998.

[13] A. Paulus, C. Winterfeldt, T. Pfeifer, D. Walter, G. Gerber, and C. Spielmann. Novel time-of-flight electron spectrometer optimized for time-resolved soft-x-ray photoelectron spectroscopy. *Review of Scientific Instruments*, 77(4):043105, 2006.

[14] Joseph Ladislas Wiza. Microchannel plate detectors. *NUCL. INSTRUM. METHODS*, 162:60—1, 1979.

[15] W. B. Colson, J. McPherson, and F. T. King. High-gain imaging electron multiplier. *Review of Scientific Instruments*, 44(12):1694 –1696, December 1973.

[16] *Polarization Optics in Telecommunications*, volume 101, chapter 4, pages 184–189. Springer-Verlag, New York, 2005.

[17] M. U. Wehner, M. H. Ulm, and M. Wegener. Scanning interferometer stabilized by use of pancharatnam's phase. *Optics Letters*, 22(19):1455–1457, October 1997.

[18] Jeffrey Moses Kyung-Han Hong Siddharth Bhardwaj Jonathan R. Birge Li-Jin Chen Enbang Li Benjamin J. Eggleton Giulio Cerullo Shu-Wei Huang, Giovanni Cirmi and Franz X. Krtner. Scalable high-energy sub-cycle waveform synthesis for strong-field physics. *Submitted to Science.*

[19] J. Mauritsson, T. Remetter, M. Swoboda, K. Klunder, A. L'Huillier, K. J Schafer, O. Ghafur, F. Kelkensberg, W. Siu, P. Johnsson, M. J. J Vrakking,

I. Znakovskaya, T. Uphues, S. Zherebtsov, M. F Kling, F. Lepine, E. Benedetti, F. Ferrari, G. Sansone, and M. Nisoli. Attosecond electron spectroscopy using a novel interferometric pump-probe technique. *1001.1085*, January 2010. Phys. Rev. Lett. 105, 053001 (2010).

[20] H Bandulet, D Comtois, E Bisson, A Fleischer, H Ppin, J Kieffer, P Corkum, and D Villeneuve. Gating attosecond pulse train generation using multicolor laser fields. *Physical Review A*, 81(1):013803, January 2010.

[21] Aurélie Jullien, Thomas Pfeifer, Mark J. Abel, Phillip M. Nagel, Justine Bell, Daniel M. Neumark, and Stephen R. Leone. Ionization gating for tunable isolated attosecond pulse generation. In *Conference on Lasers and Electro-Optics/Quantum Electronics and Laser Science Conference and Photonic Applications Systems Technologies*, page JFH7. Optical Society of America, 2008.

[22] Zenghu Chang. Controlling attosecond pulse generation with a double optical gating. *Physical Review A (Atomic, Molecular, and Optical Physics)*, 76(5):051403, 2007.

[23] I. J. Sola, E. Mevel, L. Elouga, E. Constant, V. Strelkov, L. Poletto, P. Villoresi, E. Benedetti, J.-P. Caumes, S. Stagira, C. Vozzi, G. Sansone, and M. Nisoli. Controlling attosecond electron dynamics by phase-stabilized polarization gating. *Nat Phys*, 2(5):319–322, May 2006.